PCCP

Accepted Manuscript

ROYAL SOCIETY OF CHEMISTRY

www.rsc.org/pccp

Local Environments of Boron Heteroatoms in Non-Crystalline Layered Borosilicates

Mounesha N. Garaga,[a] Ming-Feng Hsieh,[b] Zalfa Nour,[a]

Michael Deschamps,[a] Dominique Massiot,[a] Bradley F. Chmelka,[b] Sylvian Cadars[a,c,]*

[a] CNRS, CEMHTI UPR3079, Univ. Orléans, F-45071 Orléans, France

[b] Department of Chemical Engineering, University of California, Santa Barbara, California 93106, U.S.A

[c] present address: Institut des Matériaux Jean Rouxel (IMN), Université de Nantes, CNRS, 2 rue de la Houssinière, BP32229, 44322 Nantes cedex 3, France

RECEIVED DATE: July 10th, 2015

* To whom correspondence should be addressed. E-mail: sylvian.cadars@cnrs-imn.fr

TITLE RUNNING HEAD: Local Environments near Heteroatoms in Layered Borosilicates.

CORRESPONDING AUTHOR FOOTNOTE

Dr. Sylvian Cadars

Institut des Matériaux Jean Rouxel (IMN), UMR6502, Université de Nantes, CNRS,

2 rue de la Houssinière, BP32229, 44322 Nantes cedex 3, France

E-mail : sylvian.cadars@cnrs-imn.fr

Abstract

Boron heteroatom distributions are shown to be significantly different in two closely related layered borosilicates synthesized by subtly different alkylammonium surfactant species. The complicated order and disorder near framework boron sites in both borosilicates were characterized at the molecular level by using a combination of multi-dimensional solid-state nuclear magnetic resonance (NMR) spectroscopy techniques and first-principles calculations. Specifically, two-dimensional (2D) solid-state *J*-mediated (through-bond) $^{11}B\{^{29}Si\}$ NMR analyses provide direct and local information on framework boron sites that are covalently bonded to silicon sites through bridging oxygen atoms. The resolution and identification of correlated signals from distinct ^{11}B-O-^{29}Si site pairs reveal distinct distributions of boron heteroatoms in layered borosilicate frameworks synthesized with the different $C_{16}H_{33}N^{+}Me_3$ and $C_{16}H_{33}N^{+}Me_2Et$ structure-directing surfactant species. The analyses establish that boron atoms are distributed non-selectively among different types of silicon sites in the layered $C_{16}H_{33}N^{+}Me_3$-directed borosilicate framework, whereas boron atoms are preferentially incorporated into incompletely condensed Q^3-type sites in the $C_{16}H_{33}N^{+}Me_2Et$-directed borosilicate material. Interestingly, framework boron species appear to induce framework condensation of their next-nearest-neighbor silicon sites in the $C_{16}H_{33}N^{+}Me_3$-directed borosilicate. By comparison, the incorporation of boron atoms is found to preserve the topology of the $C_{16}H_{33}N^{+}Me_2Et$-directed borosilicate frameworks. The differences in boron site distributions and local boron-induced structural transformations for the two surfactant-directed borosilicates appear to be due to different extents of cross-linking of the siliceous frameworks. The molecular-level insights are supported by density functional theory (DFT) calculations, which show the distinct influences of boron atoms on the $C_{16}H_{33}N^{+}Me_3$- and $C_{16}H_{33}N^{+}Me_2Et$-directed borosilicate frameworks, consistent with the experimental observations.

KEY WORDS:

Solid-state NMR, first-principles calculations, phyllosilicates, heteroatom incorporation, atomic distributions, scalar couplings

1. Introduction

Porous materials, such as silica and zeolites, have attracted significant attention over the past decades, because of their diverse properties that have been exploited in numerous industrial applications, including as ion exchangers,[1-3] adsorbents,[4-6] separation membranes,[7, 8] or heterogeneous catalysts.[9-11] These applications substantially rely on properties that are often attributed to the presence of heteroatoms (*e.g.*, Al, B, Ga) in silica- or silicate frameworks. Consequently, understanding the influences that the type, quantity, and distributions of heteroatoms in siliceous frameworks is expected to aid improvements in the properties of such materials.[12-14] This has been a major challenge, in part because characterization of heteroatom siting is difficult. Even in porous materials with well-ordered structures, such as zeolites, it is challenging to identify the locations of heteroatoms in their frameworks, as diffraction methods tend to provide predominantly average long-range order, except for some types of heavy heteroatoms (*e.g.*, Fe or Ti).[15-17] Diffraction data of sufficiently good quality (typically using synchrotron X-rays and/or neutrons on highly-crystalline powders or on single crystals) may provide average mixed compositions for all crystallographic sites in the favorable cases where structure factors between the heteroatom and Si are different (e.g., Fe[18] or Ga,[19, 20] but not for Al[21]). Although this is typically true for boron, the degree of crystallinity and/or the amount of incorporated heteroatoms is in many cases nevertheless insufficient to obtain a reliable refinement of mixed site compositions, especially in the case of layered materials with stacking disorder. And even when the overall siting can be obtained with a good accuracy, this only corresponds to a long-range average

that provides no information on the short-range ordering and the local structural distortions that can result from the presence of these heteroatoms in the framework.[22, 23]

Solid-state nuclear magnetic resonance (NMR) spectroscopy is sensitive to the local environments of heteroatoms and their distributions in heteroatom-containing silicates, although the limited resolution of one-dimensional (1D) NMR spectra has often led to ambiguous results.[24, 25] Previous investigations have suggested near-random[19] or relatively unselective distributions of heteroatoms in zeolite frameworks.[12, 25-29] Zeolites with three-dimensional (3D) structures are composed of four-coordinate Si or heteroatom sites (so-called "tetrahedral" sites or "T-sites") that are bonded to other four T-sites via bridging oxygen atoms, which lead to solid-state ^{29}Si NMR signals that are designated as Q^4 ^{29}Si species. (The Q^n notation describes bonding configurations of T-sites, where n refers to the number of connected T-sites for a given T-site.) Incompletely condensed Q^3 ^{29}Si sites are in general only present in zeolites in the form of defects, with the exception of a few zeolites where ordered (intrinsic) vacancies have recently been revealed.[30, 31] In siliceous zeolites with 3D crystalline order, subtle differences in Si-O-Si bond angles and lengths lead to ^{29}Si signals that can be resolved from crystallographically distinct T-site environments. However, heteroatoms inserted into these Q^4 ^{29}Si sites appear to result into ^{29}Si NMR signals that are difficult to resolve, making it challenging to determine the locations of heteroatoms in the frameworks. In rare cases, heteroatoms are incorporated into specific framework sites (*e.g.*, B in the borosilicate zeolite MCM-70[32] and layered borosilicate RUB-39,[33] Al[21, 34] or Ga[35] in natrolite-type zeolites), leading to resolved NMR signals. However, heteroatoms are more typically incorporated into silicate frameworks without detectable extents of long-range order, leading to broad signals that provide little information on the distinct local heteroatom environments or their distributions.

In contrast to most zeolites, the ordered 2D frameworks of layered silicates contain incompletely condensed Q^3 ^{29}Si framework moieties that are generally intrinsic to their structure, in addition to fully condensed Q^4 sites.[36-45] Such Q^3 and Q^4 ^{29}Si species yield ^{29}Si NMR signals over different frequency ranges: *ca.* -92 to -103 ppm and *ca.* -105 to -120 ppm, respectively. Among different types of layered silicates, surfactant-directed layered silicates[46, 47] provide several different types of Q^3 and Q^4 ^{29}Si framework sites into which heteroatoms can be incorporated and potentially distinguished. Here, we focus on surfactant-directed layered silicates that are synthesized in presence of cationic alkylammonium surfactants $CH_3(CH_2)_{15}N^+Me_3$ or $CH_3(CH_2)_{15}N^+Me_2Et$, where Me = -CH_3 and Et = -C_2H_5;[46] these different surfactant head groups lead to siliceous frameworks with different structures containing one Q^3 and one Q^4 ^{29}Si sites or two Q^3 and 3 Q^4 ^{29}Si sites, respectively. Furthermore, solid-state ^{29}Si NMR signals for these two layered silicate materials are well resolved and expected to facilitate characterization of distributions of heteroatoms incorporated into their frameworks. Al heteroatoms have previously been incorporated in the $C_{16}H_{33}N^+Me_3$ - directed layered silicate material, which led to the creation within the framework of acidic sites whose location could not be clearly established from standard 1D NMR measurements[48, 49] In this work we investigate the intercalation of B heteroatoms into both $CH_3(CH_2)_{15}N^+Me_3$ or $CH_3(CH_2)_{15}N^+Me_2Et$ – directed borosilicate. The weaker acidity of incorporated B as compared to Al heteroatoms opens the way to a modulation of the acid catalytic properties for reactions requiring mild acidic solid catalysts.[50, 51] In addition, Borosilicate zeolites be post-synthetically modified by isomorphic substitution of B by other heteroatoms to prepare zeolites that are difficult to synthesize directly.[52, 53]

Among the main strengths of NMR spectroscopy is the ability to unambiguously establish the existence of chemical bonds, which are probed through indirect spin-spin couplings between nuclei, also referred to as *J* couplings. Reviews on the methods to probe

and use these couplings in solids have been published.[54, 55] They have been used for many years in zeolites, layered and other types of silica(tes) materials to probe Si-O-Si[46, 47, 56-59] or Si-O-Al[60-62] connectivities in the form of through-bond mediated two-dimensional correlation experiments or spin-counting experiments.[61] In addition to shedding light on local framework topologies, this is extremely valuable information, particularly when combined with molecular modeling (at the density functional level of theory, DFT), to assist structure determination or refinement,[63-65] or even describe T-O-T bond angle distributions in the presence of geometrical disorder.[66] These methodologies furthermore offer the opportunity to identify and/or spectrally resolve otherwise overlapping local environments based on their connectivities, to then distinguish between such variations in the local bonding geometry (geometric disorder) and disorder of chemical origins, such as atomic substitutions.[23, 67, 68]

Here, B atom site distributions in $C_{16}H_{33}N^{+}$**Me$_3$-** and $C_{16}H_{33}N^{+}$**Me$_2$Et**-directed layered borosilicates are established and shown to be significantly different. Specifically, the complicated order and disorder near B sites were probed using a combination of solid-state multi-dimensional NMR techniques and DFT calculations. Importantly, our results reveal significantly different B site distributions in the two surfactant-directed borosilicates synthesized under otherwise identical compositions and conditions.

2. Results and Discussion

2.a. Average long-range structures from diffraction and elemental analyzes. The locations of boron atoms in surfactant-directed layered silicates are exceedingly difficult to elucidate, because they exhibit less extents of long-range order than crystalline structures. Such characteristics make diffraction-based analyses, which are sensitive to long-range framework order, less suitable for this task. For example, powder X-ray diffraction (XRD) patterns of as-synthesized $C_{16}H_{33}N^{+}$**Me$_3$-** and $C_{16}H_{33}N^{+}$**Me$_2$Et**-directed borosilicates (with

natural ^{29}Si abundance) show small- (Figure 1a,c) and high-angle reflections (Figure 1b,d) in both borosilicate materials, indicating a high degree of mesoscopic lamellar order and long-range framework order, respectively. The mesoscopic lamellar ordering was visually confirmed elsewhere by high resolution transmission electron microscopy for the siliceous analog of the $C_{16}H_{33}N^+$**Me$_2$Et**-directed borosilicate material studied here,[64] which also yields identical XRD and ^{29}Si NMR (see below) signatures.[47] The XRD pattern of the $C_{16}H_{33}N^+$**Me$_3$**-borosilicate is also similar to the one obtained for the siliceous analog.[46] Basal distances of ca. 3.7 and 3.2 nm extracted from the low-angle reflections for the $C_{16}H_{33}N^+$**Me$_2$Et**- and $C_{16}H_{33}N^+$**Me$_3$**-borosilicate materials, respectively, indicate similarly high extents of vertical alignment (*i.e.,* perpendicular to the layers) of the surfactant hydrophobic tails. In contrast with these reference silicate materials, however, bulk elemental analyses summarized in Table 1 reveal the presence of boron in the two materials whose XRD patterns are shown in Figure 1. The $C_{16}H_{33}N^+$**Me$_3$**- and $C_{16}H_{33}N^+$**Me$_2$Et**-directed borosilicate materials are shown to have Si/B ratios of 142 and 52, respectively. Based on the XRD and elemental analyses, B incorporation does not appear to induce substantial changes of long-range order in $C_{16}H_{33}N^+$**Me$_3$**- and $C_{16}H_{33}N^+$**Me$_2$Et**-directed layered borosilicates, as compared to their siliceous counterparts. However, it is not possible to establish the locations of B atoms in the two borosilicate frameworks by using XRD analyses alone. Consequently, distributions of B sites, as well as their interactions with structure-directing surfactant species and silicon framework sites have still remained elusive.

2.b. Short-range molecular structures from ^{29}Si NMR data. As the XRD analyses that show a high degree of similarity between $C_{16}H_{33}N^+$**Me$_3$**- and $C_{16}H_{33}N^+$**Me$_2$Et**-directed layered borosilicates and siliceous materials, 1D ^{29}Si{^{1}H} CP-MAS NMR of $C_{16}H_{33}N^+$**Me$_3$**- and $C_{16}H_{33}N^+$**Me$_2$Et**-directed layered borosilicates reveals two and five ^{29}Si species, as

shown in Figure 2a,c, respectively. Interestingly, the 1D ^{29}Si NMR analyses appear to be identical to the associated siliceous counterparts, where $C_{16}H_{33}N^{+}$**Me$_3$-** and $C_{16}H_{33}N^{+}$**Me$_2$Et-**directed layered silicates have two and five distinct ^{29}Si framework sites, respectively.[46, 47] The results indicate that short-range molecular order of the borosilicate and siliceous frameworks are very similar. Furthermore, the narrow ^{29}Si NMR spectral widths (full-width-at-half-maximum (FWHM): 0.8 to 1.5 ppm) in Figure 2a,c show highly uniform local ^{29}Si environments present in both surfactant-directed borosilicates. Specifically, $C_{16}H_{33}N^{+}$**Me$_3$-**directed borosilicate has one Q^3 and one Q^4 ^{29}Si species, designated as Si1 and Si2, respectively, with the Q^3/Q^4 ratio of 0.50. By comparison, two Q^3 (Si1 and 2) and three Q^4 ^{29}Si species (Si3, 4, and 5) are present in the $C_{16}H_{33}N^{+}$**Me$_2$Et**-directed borosilicate with the approximate Q^3/Q^4 ratio of 0.67. Two-dimensional experiments probing the existence of ^{29}Si-O-^{29}Si linkages, which are shown in Supporting Information Figure S1 and described in the corresponding captions, also indicate that the topologies (i.e. coordination sequences and ring structures) are also identical in the borosilicate and the siliceous analogs. Nevertheless, the ^{29}Si NMR analyses do not provide information that may be directly linked to the possible presence of B species in the frameworks of either of the surfactant-directed borosilicate materials.

2.c. Probing the local structure around boron heteroatoms with ^{11}B NMR spectroscopy. In contrast with XRD and ^{29}Si NMR analyses, ^{11}B NMR spectroscopy provides local information on ^{11}B species in borosilicates. For example, 1D ^{11}B echo-MAS reveals three and one four-coordinate ^{11}B sites in the $C_{16}H_{33}N^{+}$**Me$_3$-** and $C_{16}H_{33}N^{+}$**Me$_2$Et**-directed layered borosilicates, as evidenced by various ^{11}B NMR signals (FWHM: 0.3 to 0.5 ppm) in Figure 2b and d, respectively. Both $C_{16}H_{33}N^{+}$**Me$_3$-** and $C_{16}H_{33}N^{+}$**Me$_2$Et**-directed silicate structures being composed of four-coordinate framework Si sites only, B species (and by

extension ^{11}B nuclei) incorporated in the framework, in substitution of any of these sites, would become four-coordinated as well. In this regard, B incorporation is expected to modify the host inorganic structures, primarily because of different sizes between Si and B atoms, but also because of their different valence states, which will imply a local charge-compensation mechanism around incorporated B atoms. To support such a hypothesis, the elemental analyses (*i.e.*, Si/B ratios) were used to estimate the possible fraction of ^{29}Si NMR signals that result from ^{29}Si sites near ^{11}B species and are therefore expected to differ from the signature of the corresponding reference silicate systems. The detailed description and results are summarized in Table S1. Specifically, the results indicate that more than 15% of the ^{29}Si NMR signals would be affected if substantial influences of ^{11}B sites on their neighboring ^{29}Si species exist in the $C_{16}H_{33}N^+$**Me$_2$Et**-directed borosilicate (assuming for instance a perturbation range of 5 Å or more). However, this estimation is in stark contrast with the 1D ^{29}Si NMR spectrum (Figure 2c), showing that the $C_{16}H_{33}N^+$**Me$_2$Et**-directed borosilicate has very similar ^{29}Si environments to its siliceous analog. Such facts suggest that framework B species exhibit highly localized influences on their nearby ^{29}Si neighbors (very likely less than 5 Å). The ^{11}B NMR analyses demonstrate a single type of well-defined ^{11}B environment (0.3 ppm fwhm, Fig. 2d) and suggest that B atoms seem to incorporate into one type of Si sites in the $C_{16}H_{33}N^+$**Me$_2$Et**-directed borosilicate. This is possibly a similar situation to the case of crystalline layered borosilicate RUB-19, of composition $[Si_9O_{18}(OH)][Me_2Pr_2N^+]\bullet xH_2O$,[33] for which the authors concluded that the small amount of B atoms incorporated were preferentially sitting in a single T site based on a relatively sharp (ca. 1 ppm fwhm) dominant ^{11}B NMR peak and XRD data. Interestingly the single ^{11}B NMR line observed here for the $C_{16}H_{33}N^+$**Me$_2$Et**-directed borosilicate is significantly sharper (0.3 ppm fwhm), further supporting the interpretation of a site-specific incorporation.

Very different from the case of $C_{16}H_{33}N^{+}$**Me$_2$Et**-directed borosilicate, 1D ^{11}B NMR analyses provide solid evidence that framework B species induce structural changes in the $C_{16}H_{33}N^{+}$**Me$_3$**-directed borosilicate frameworks. Specifically, three ^{11}B signals at -0.9, -1.9, and -2.5 ppm are identified by the 1D ^{11}B NMR (Figure 2b), all of which correspond to three distinct four-coordinate ^{11}B sites, designated as B1, B2, and B3, respectively. This obviously exceeds the number of distinct framework Si sites (two) available for B incorporation, indicating that structural rearrangements occur in the $C_{16}H_{33}N^{+}$**Me$_3$**-directed borosilicate frameworks upon ^{11}B incorporation. While distinct ^{11}B species are resolved and identified by 1D ^{11}B NMR, their exact locations and B-induced structural modifications in both surfactant-directed borosilicate materials have still remained elusive.

Molecular interactions that involve ^{11}B species and their neighboring ^{1}H species were measured to provide insights about B site distributions in both surfactant-directed borosilicate materials. B atoms inserted into Q^3 and Q^4 ^{29}Si sites, designated as Q^3 and Q^4 B species, respectively, are indeed expected to have different extents of influences of ^{1}H species. Q^3 ^{11}B sites would typically interact more strongly with ^{1}H species than Q^4 ^{11}B sites, due to the fact that Q^3 ^{11}B sites bonded to negatively-charged non-bridging O atoms would be charge balanced either by a proton coming from the reaction medium and forming a hydroxylated B-O-H species, or by positively-charged headgroups of alkylammonium surfactants. Various spatial proximities between ^{1}H and ^{11}B species could be distinguished by measuring transverse ^{11}B dephasing times T_2' (*i.e.*, rate of signal loss during a spin echo) in presence or absence of heteronuclear ^{11}B-^{1}H decoupling.[69, 70] The results are presented in Supporting Information, Figure S2 and summarized in Table 2 for both surfactant-directed borosilicate materials. In the case of the $C_{16}H_{33}N^{+}$**Me$_3$**-directed borosilicate, ^{11}B sites B1 and B2 show identical T_2' (*i.e.*, 24 ms) in the presence of heteronuclear ^{11}B-^{1}H decoupling. (Low ^{11}B signal sensitivity and limited spectral resolution for ^{11}B site B3 prevent reliable T_2' measurements.)

In contrast, ^{11}B sites B1 and B2 exhibit significantly different T_2' times, 7.0 and 16 ms, respectively, in the absence of ^{1}H decoupling, indicating that magic-angle-spinning alone is insufficient to remove all the heteronuclear ^{11}B dipole-^{1}H dipole interactions. Residual ^{1}H-^{11}B couplings consequently affect T_2' times of the ^{11}B sites B1 and B2, revealing large differences that indicate that ^{11}B site B1 is under greater influences from ^{1}H species than ^{11}B site B2. As such, the ^{11}B site B1 can be attributed to B atoms incorporated into Q^3 ^{29}Si sites, and ^{11}B site B2 refers to B atoms substituted into Q^4 ^{29}Si sites. The similar ^{11}B shifts of the ^{11}B sites B2 and B3 suggest that ^{11}B site B3 seems to stem from B atoms incorporated into Q^4 ^{29}Si site. Similarly, in the case of the $C_{16}H_{33}N^+$**Me$_2$Et**-directed borosilicate, the ^{11}B signal shows very different T_2' times that are 35 and 4.0 ms measured in the presence and absence of ^{11}B-^{1}H decoupling, establishing that the associated four-coordinate ^{11}B sites result from the B atoms incorporated into Q^3 ^{29}Si sites.

In addition, 2D dipolar-mediated (through-space) ^{11}B{^{1}H} NMR analyses provide local information on ^{11}B sites that are molecularly proximate to their neighboring ^{1}H species (< 1 nm) in the $C_{16}H_{33}N^+$**Me$_3$**- and $C_{16}H_{33}N^+$**Me$_2$Et**-directed layered borosilicates, as shown in Figure 3a and b, respectively. For example, both 2D ^{11}B{^{1}H} NMR spectra reveal correlated intensities among all ^{11}B signals and one ^{1}H signal (at *ca.* 3.5 ppm) that corresponds to ^{1}H species of surfactant headgroups (*i.e.*, N-C**H$_3$** and/or N-C**H$_2$**). Such strong intensity correlations show that the four-coordinate ^{11}B species are molecularly proximate to surfactant headgroups in both materials, as illustrated as insets in red in Figure 3a and b. These spatial proximities are characteristic of the strong electrostatic organic-inorganic interactions that govern the formation of surfactant-directed materials,[46] and are consistent with the similar propensity of the surfactant tails in both materials to lie perpendicular to the layers, as inferred from the similarly high basal distances. Interestingly, in the case of the $C_{16}H_{33}N^+$**Me$_3$**-directed borosilicate, the ^{11}B signal at -0.9 ppm (^{11}B site B1) exhibits

correlation intensities with the relatively weak ^{1}H signal at 1.9 ppm associated with the second CH_2 group in the alkyl chain of $C_{16}H_{33}N^{+}$**Me$_3$** surfactant molecules, as shown in blue in Figure 3a. By comparison, other ^{11}B signals at -1.9 and -2.5 ppm (^{11}B sites B2 and B3, respectively) do not reveal correlations with such a ^{1}H signal at 1.9 ppm. These differences demonstrate that ^{11}B site B1 interact more strongly with ^{1}H moieties than ^{11}B sites B2 and B3, consistent with the analyses of T_2' measurements. Similarly, in the case of the $C_{16}H_{33}N^{+}$**Me$_2$Et**-directed borosilicate, the ^{11}B signal at -0.4 ppm (^{11}B site B1) is also correlated with the ^{1}H signal at 1.9 ppm, corresponding to the second CH_2 group in the alkyl chain of $C_{16}H_{33}N^{+}$**Me$_2$Et** surfactant molecules, and highlighted in blue in Figure 3b. Furthermore, the ^{11}B signals at -0.9 and -0.4 ppm (in $C_{16}H_{33}N^{+}Me_3$- and $C_{16}H_{33}N^{+}Me_2Et$-directed borosilicate respectively) both show correlation intensities with a ^{1}H signal at *ca*. 1 ppm associated with B-OH or B-(OH)-Si moieties, highlighted in green in Figure 3a and b, respectively. These correlations indicate that these ^{1}H species arise from ^{11}B atoms incorporated in Q^3 Si sites and consequently represent a small fraction of all the ^{1}H moieties present in the $C_{16}H_{33}N^{+}$**Me$_3$**- and $C_{16}H_{33}N^{+}$**Me$_2$Et**-directed layered borosilicates given the low B contents (Si/B ratios of *ca.* 50 or more). 2D ^{11}B{^{1}H} NMR analyses provide such molecular-level insights about charge compensation of anionic B sites in the borosilicate frameworks and are helpful for establishing models of the distorted local structures around these ^{11}B sites.

2.d. Modeling approaches to describe possible local structures around incorporated Boron heteroatoms. Molecular modeling can yield information about such short-range order and disorder near B sites in the $C_{16}H_{33}N^{+}$**Me$_3$**- and $C_{16}H_{33}N^{+}$**Me$_2$Et**-directed layered borosilicates to support the NMR analyses. In particular, calculation of NMR parameters using density functional theory (DFT) is a powerful means to validate structural models. DFT

calculations were conducted on representative models of both surfactant-directed borosilicates to examine and evaluate possible order and disorder near framework B species in both surfactant-directed borosilicates, which can be described by (periodic) models that consist of a single 2D borosilicate sheet, because the presence of flexible and mobile surfactants in the inter-layer space of these layered materials results in a high degree of stacking disorder. Our $C_{16}H_{33}N^{+}$**Me$_3$**-directed silicate models were based on the octosilicate structure[71] that possesses similar ^{29}Si-NMR signatures to the $C_{16}H_{33}N^{+}$**Me$_3$**-directed silicate.[46, 72] There are two distinct types of Q^4 and Q^3 ^{29}Si sites (labeled as T1 and T2) in the octosilicate corresponding to ^{29}Si sites Si2 and Si1 in the $C_{16}H_{33}N^{+}$**Me$_3$**-directed layered silicate, respectively. On the other hand, advanced NMR-based structure determination protocols led to the identification of three equally valid candidate framework models of the $C_{16}H_{33}N^{+}$**Me$_2$Et**-directed silicate,[64] all of which were considered in our calculations. This silicate framework was also found to be identical to the individual layers of two newly reported materials HUS-2 of composition (per unit cell) $[Si_{20}O_{40}(OH)_4]^{4-}[HO\text{-}(CH_2)_2\text{-}N^{+}Me_3]_4 \bullet 1.03(H_2O)$ [73] and CLS-1 of composition $[Si_{20}O_{40}(OH)_4]^{4-}[Me_2N\text{-}C_5H_4N^{+}\text{-}Et]_4 \bullet 7.6(H_2O)$,[65] which exhibit substantially higher extents of long-range inter-layer stacking order (albeit incomplete in CLS-1[65]). Elemental analyzes (Table 1) indicate that the samples contain between 0.6 and 0.7 surfactant molecules per Q^3 groups. This means that, in analogy to the cases of octosilicate, HUS-2, and CLS-1 materials,[65, 72, 73] the rest of the negative charges of non-bridging O atoms is compensated in both borosilicates studied here by protons forming a strong Si-O-H···O-Si hydrogen-bonds between two adjacent Q^3 Si sites, leading primarily to $[Si_5O_{10}(OH)]^{-}$ formula units for the framework. These protons, which are characterized by ^{1}H NMR peaks in the 13-16 ppm range in (at least partly) crystalline layered silicates octosilicate, HUS-2 and CLS-1, have never been clearly observed in the isostructural surfactant-directed silicates. This is probably because they are considerably more mobile in

the latter at room temperature and are potentially also exchanging with nearby $Si_5O_{11}^{2-}$ units, which causes their ^{1}H NMR resonance frequencies to be distributed across a large part of the ^{1}H frequency range as a result of distributions of H-bond lengths, such that they are hidden in the feet of other ^{1}H NMR peaks.

The basic idea of our modeling approach is to replace one Si atom by a B atom in supercells made from the reference $C_{16}H_{33}N^+$**Me$_3$**- and $C_{16}H_{33}N^+$**Me$_2$Et**-directed silicate systems to then evaluate these borosilicate models and study the effect of the Si to B substitution on the framework structure. The difficulty here resides in the strategies used for the compensation of the negative charges associated with the non-bridging O atoms (those not compensated by a proton) and the incorporated B atom. Two different approaches were tested to model the alkylammonium surfactant molecules. In the first, unsuccessful, approach described in Supporting Information (Figures S3 and S4, Tables S2 and S3), surfactants with relatively short alkyl chains, such as CH_3-$(CH_2)_3$-N^+**Me$_3$** or CH_3-$(CH_2)_3$-N^+**Me$_2$Et** molecules, were included in the inter-layer space of all candidate structure models to mimic charge-compensating surfactant molecules. While ^{11}B NMR chemical shifts calculated with this method seem reasonably reliable, calculated ^{29}Si chemical shifts are not consistent with the experimental NMR analyses. It has been established before that freezing the surfactant-headgroup motions by decreasing temperature has strong impacts on ^{29}Si NMR signals.[74] The frozen states of the surfactant-mimicking molecules in our models are therefore not representative of the mobile surfactants and their dynamically-averaged influence on the electronic structure of borosilicate layers at room temperature.

In an alternative approach to model the complicated organic-inorganic interactions and their influence on the ^{29}Si and ^{11}B NMR signatures, the surfactant molecules were omitted and replaced by positive charges homogenously distributed across the entire unit cell. This strong approximation was first validated for the siliceous systems, as illustrated in Figure S5.

Best results were obtained with calculations conducted on model unit cells that contain one H atom per pair of non-bridging O atoms, corresponding to reference compositions $[Si_8O_{16}(OH)_2]^{2-}$ in the case of the $C_{16}H_{33}N^+$**Me$_3$**-directed silicate, $[Si_{10}O_{20}(OH)_2]^{2-}$ for the $C_{16}H_{33}N^+$**Me$_2$Et**-directed silicate. Such configurations would lead to borosilicates with 0.5 charge-compensating surfactant molecule per Q^3 unit, which is reasonably close to the elemental analyses of both surfactant-directed borosilicates (see Table 1). This modeling strategy appears to substantially improve the agreement between experimental and calculated NMR parameters in the case of $C_{16}H_{33}N^+$**Me$_2$Et**-directed silicates, as compared to the previously used approximation,[64] where all non-bridging oxygen atoms were protonated to form silanol groups. Importantly, these calculations further validate the three "equally-valid framework structural models" that were previously established,[64] two of which (structural models 2 and 4 using the designation of ref. 64) appear to converge to a single structure when only two of their non-bridging oxygen atoms are protonated. Structural models 2 and 3, obtained after optimization with 2 H atoms per supercell, were consequently considered reference systems to construct a second series of models of the $C_{16}H_{33}N^+$**Me$_2$Et**-directed borosilicates. In both series of systems, B atoms were then introduced by replacing one Si atom in a 2x2x1 supercell, corresponding to models of compositions $[BSi_{39}O_{80}(OH)_8]^{9-}$ for the $C_{16}H_{33}N^+$**Me$_2$Et**-directed borosilicates, and $[BSi_{31}O_{64}(OH)_8]^{9-}$ for the $C_{16}H_{33}N^+$**Me$_3$**-directed borosilicates, as reported in Table 3, and in the first two rows of Table 4, respectively.

2.e. Evaluations of $C_{16}H_{33}N^+Me_2Et$-directed borosilicate models: calculated NMR data vs. advanced experimental correlation NMR data. Calculated NMR parameters obtained from the second modeling approach appear to be more reliable than the first approach. Figure 4a shows a representative structural model of the $C_{16}H_{33}N^+$**Me$_2$Et**-directed borosilicate

(viewed from *c*-axis) after DFT geometry optimization. This model was built from the reference silicate framework structure 2 (Fig. S5) in a 2x2x1 supercell, where one Si site Si1 was replaced by one B atom to form a B-OH unit. The resulting calculated ^{11}B chemical shifts, including the ones with B atoms incorporated into one of the five distinct Si sites in candidate framework structures 2 and 3, are summarized in Table 3. Interestingly, these calculations match well-separated ranges of ^{11}B chemical shifts for B atoms located in Q^3 (-0.8 to 0.9 ppm) or Q^4 sites (-2.8 to -4.1 ppm). More importantly, the range of calculated ^{11}B NMR signals for Q^3 ^{11}B sites corresponds well to the experimental ^{11}B signal at -0.4 ppm attributed to a BOH moiety formed by substitution of a Q^3 ^{29}Si site in the $C_{16}H_{33}N^+$**Me$_2$Et**-borosilicates (Figure 2d).

This modeling approach, where surfactants are omitted, also considerably improves the reliability of ^{29}Si NMR calculations as compared to the models with included surfactant-mimicking molecules. The calculated ^{29}Si chemical shifts for Q^n ^{29}Si sites (i.e. ^{29}Si sites that are not connected to a B atom), shown in black in Figure 4c, are all in good agreement with the experimental results (Figure 4b). The ^{29}Si chemical shifts calculated for ^{29}Si sites neighboring the B atoms, Q^n(1B) sites Si2, Si3, and S5, shown in yellow in Figure 4c, also compare well to experimental data (Figure 4d) that was obtained from advanced multi-dimensional solid-state NMR techniques, and which will be discussed in further detail below. The structural rearrangements induced by B incorporation may be probed through differences of the ^{29}Si chemical shifts between corresponding ^{29}Si sites calculated in the borosilicate and siliceous framework model, which are plotted in Figure 4e. The qualitative influences of an isolated B atom on its nearby ^{29}Si sites in terms of proximities are highlighted in grey in Figure 4e. The shift difference is surprisingly weak for the ^{29}Si sites with a next-nearest neighbor replaced by a B atom (the Q^3(1B) species within the black ellipse in Fig. 4e), which may be explained by a compensation between the effect due to the difference of

electronegativity between Si and B and the local geometrical rearrangements caused by the smaller size of the B atom. T-O bond lengths, T-O-T bond angles and T-O-H---O-T hydrogen bond strengths all influence ^{29}Si chemical shifts[37] in ways which appear here to oppose to the expected effect of the change in electronegativity between Si and B (in analogy to the well-known systematic effect of Si to Al substitutions). This structural model with the B atom incorporated in one specific Q^3 Si site appears to match with all the experimental data discussed so far. Similar calculations conducted for the other models, with B atoms incorporated in ^{29}Si site Si2 and/or using candidate structure no. 3 as the reference silicate framework structure, will be discussed further below, in relation to the identification of the crystallographic site on which the B atom is siting. For this, however, it is first necessary to explain how the experimental ^{29}Si spectrum of Figure 4d featuring selectively Q^n(1B) species was obtained.

The specific signature ^{29}Si nuclei connected to ^{11}B nuclei through bridging O atoms exploits the unique ability of solid-state NMR spectroscopy to provide two-dimensional (2D) correlation experiments that are mediated though the $^2J(^{11}\text{B-O-}^{29}\text{Si})$ scalar couplings. Figure 5a shows in red a 2D $^2J(^{11}\text{B-O-}^{29}\text{Si})$-mediated Heteronuclear Multiple-Quantum Correlation (HMQC) ^{11}B{^{29}Si} NMR spectrum of a $C_{16}H_{33}N^+$**Me$_2$Et**-directed layered borosilicate material prepared with *ca.* 99% enrichment in ^{29}Si. The 1D ^{11}B echo-MAS and ^{29}Si{^{1}H} CP-MAS spectra of this ^{29}Si-enriched material are shown along the top horizontal and the right vertical axis of the 2D ^{11}B{^{29}Si} spectrum. Both are similar to the 1D spectra of the corresponding $C_{16}H_{33}N^+$**Me$_2$Et**-directed layered borosilicate with natural abundance of ^{29}Si (Figure 2c,d), except for the presence of a boron-containing impurity (marked with a star in the 1D ^{11}B echo-MAS spectrum). Various correlated intensities in this 2D ^{11}B{^{29}Si} NMR spectrum (Fig. 5a, in red) reveal different ^{29}Si sites covalently bonded to ^{11}B atoms via bridging oxygen atoms in the borosilicate framework. It is the ^{29}Si projection of this 2D

spectrum, shown in red on the right of Figure 5a, that was included in Figure 4d for direct comparison with calculated ^{29}Si chemical shifts corresponding to Q^n(1B) ^{29}Si environments. Because they lack a ^{11}B-O-^{29}Si connection, ^{29}Si Q^n sites are indeed totally filtered out in the 2D correlation spectrum, and thus in its ^{29}Si projection. Details of the 2D spectrum reveal three distinct ^{29}Si signals at -98.4, -100.5 and -113.8 ppm that are correlated with one ^{11}B signal at -0.4 ppm. As mentioned above, the small broadening of this ^{11}B signal suggests a highly uniform single type of ^{11}B environments. Consequently, the three types of ^{29}Si-O-^{11}B correlations indicate that every incorporated B atom is connected to three distinct Si atoms (Q^3(1B) or Q^4(1B)) via bridging oxygen atoms. Specifically, two of the three Q^n(1B) ^{29}Si sites revealed in the *J*-mediated ^{11}B{^{29}Si} correlation NMR spectrum fall within a region of the ^{29}Si spectrum that is compatible with Q^3(1B) signatures, consistent with the connectivities established from the siliceous counterpart, where each Q^3 ^{29}Si site is connected to another Q^3 ^{29}Si site. Such information allows us to confirm that the ^{11}B signal at -0.4 ppm can be attributed to B atoms incorporated into one of the two types of Q^3 Si sites. Additionally, the local topology near B sites in the $C_{16}H_{33}N^+$**Me$_2$Et**-directed borosilicate does not appear to rearrange during framework crystallization. As will be discussed further below this is in stark contrast with the case of the $C_{16}H_{33}N^+$**Me$_3$**-directed borosilicate material which will be discussed further below.

While the 2D *J*-mediated (through-bond) ^{11}B{^{29}Si} NMR analyses provide specific information on the ^{11}B sites that are covalently bonded to the next-nearest-neighbor ^{29}Si sites, ^{29}Si sites in the first coordination shells may be spatially close to ^{11}B sites in the $C_{16}H_{33}N^+$**Me$_2$Et**-directed layered borosilicate framework, which can be revealed via 2D dipolar-mediated ^{11}B{^{29}Si} NMR experiments. Figure 5a shows in blue a 2D dipolar-mediated HMQC ^{11}B{^{29}Si} NMR spectrum of the *ca.* 99% ^{29}Si-enriched $C_{16}H_{33}N^+$**Me$_2$Et**-directed layered borosilicate. Intensity correlations that involve the impurity, identified by the

^{11}B signal at *ca.* 4 ppm in the 1D ^{11}B NMR spectrum, are resolved with this 2D dipolar-mediated ^{11}B{^{29}Si} NMR technique, but they are distinguishable from the NMR signature of the layered borosilicate. The ^{11}B signal at *ca.* -0.4 ppm exhibits intensity correlations with the ^{29}Si signals at -98.4, -100.5 and -113.8 ppm in the 2D dipolar-mediated ^{11}B{^{29}Si} NMR spectrum (in blue, Figure 5a), consistent with the 2D *J*-mediated ^{11}B{^{29}Si} NMR spectrum (in red, Figure 5a), because of the short distances (*ca*. 3 Å) between the ^{29}Si-O-^{11}B site pairs. More importantly, additional correlated intensities are shown between the ^{11}B signal at -0.4 ppm and the ^{29}Si signals at -111.3 and -108.6 ppm, as well as a shoulder at *ca.* -101.0 ppm, all of which correspond to ^{29}Si sites that are molecularly proximate to (*ca*. 5 Å or less) yet not connected with the ^{11}B sites. Interestingly, the ^{29}Si signals at -108.6 and -101.0 ppm are very close to the ^{29}Si signals at -108.7 and -100.7 ppm, associated with ^{29}Si sites Si4 and Si2, respectively. Both ^{29}Si sites Si4 and Si2 in the $C_{16}H_{33}N^{+}$**Me$_2$Et**-directed layered borosilicate exhibit similar ^{29}Si signals to the ^{29}Si sites Si4 and Si2 (-109.1 and -101.0 ppm) in the closely related $C_{16}H_{33}N^{+}$**Me$_2$Et**-directed siliceous framework,[46] suggesting that the presence of ^{11}B atoms subtly modifies their nearby ^{29}Si environments. Similarly, another correlation that involves the ^{29}Si signal at -111.3 ppm could be attributed to ^{29}Si site 5, whose ^{29}Si chemical shift is slightly displaced with respect to the main one at -114.7 ppm due to its proximity to the ^{11}B sites. These 2D NMR analyses indicate that the ^{11}B incorporation would induce subtle influences on the ^{29}Si sites neighboring B atoms, within a small region of less than *ca.* 5 Å radius.

A direct consequence of the preservation of the framework topology and of such minor geometric distortions is a high degree of local molecular order near the B sites, as revealed by the narrow linewidths in both ^{11}B and ^{29}Si dimensions of the 2D ^{11}B{^{29}Si} NMR spectra of the $C_{16}H_{33}N^{+}$**Me$_2$Et**-directed borosilicates (Figure 5a). Specifically, the narrow linewidths of the ^{11}B signals (FWHM: 0.3 ppm) and the ^{29}Si signals (FWHM: 1.0 ~ 1.6 ppm) all reveal

well-defined local ^{11}B and ^{29}Si environments, respectively, rather than distributions of local bonding geometries. By comparison, typical linewidths of ^{11}B and ^{29}Si signals observed in borosilicate glasses are of the order of 4 ppm for four-coordinate ^{11}B species and 10 ppm for Q^3 or Q^4 ^{29}Si environments.[75] The narrow linewidths as well as 2D ^{11}B{^{29}Si} NMR analyses clearly indicate that all ^{11}B nuclei are preferentially inserted into one type of Q^3 Si sites (*i.e.*, Si1 or Si2) in the $C_{16}H_{33}N^+$**Me$_2$Et**-directed borosilicate, and lead to very similar and localized influences on their local ^{29}Si environments in this material. Additionally, these B sites can be considered to be well isolated from each other, due to the Si/B molar ratio on the order of 50. Therefore, a substantial fraction of framework sites remain occupied by Si atoms, which suggests that B atoms are distributed in a random manner, rather than periodically (*e.g.*, every unit cell) in the $C_{16}H_{33}N^+$**Me$_2$Et**-directed borosilicate framework. The ^{11}B site distributions in the proposed structure are depicted schematically in Figure 5b, where B atoms exhibit poor or no periodicity in their long-range order and yet strong similarity in subtle influences that they exert locally on the borosilicate frameworks.

The case of the $C_{16}H_{33}N^+$**Me$_2$Et**-directed borosilicate is significantly different from the case, for instance, of borosilicate zeolite MCM-70 (crystal code MVY[76]) of composition $[Si_{10}B_2O_{24}]^{2-}[K^+]_2 \cdot 2(H_2O)$ that contains four distinct crystallographic tetrahedral Si sites, three of which are exclusively occupied by Si atoms, whereas the fourth is only occupied by B atoms, as established by X-ray diffraction analyses.[32] To our knowledge, there is no evidence that a siliceous MCM-70 structure can be formed, where this crystallographic site would be occupied (even partially) by Si atoms in the average long-range structure. The situation is completely different here, first because the $C_{16}H_{33}N^+$**Me$_2$Et**-directed borosilicate lacks the 3D (and even long-range 2D) periodicity, while possessing molecular order. Second, the B loadings are small enough so that B sites can be considered to be independent of each other. Based on the understanding of local order and disorder near B sites in the

$C_{16}H_{33}N^{+}$**Me$_2$Et**-directed borosilicate, we anticipate that corresponding physico-chemical properties of all B sites in the material should be similar.

2.g. Boron sitting in the $C_{16}H_{33}N^{+}Me_2Et$-directed borosilicate material. Understanding the incorporation of boron atoms into Q^3 ^{29}Si sites in the $C_{16}H_{33}N^{+}$**Me$_2$Et**-directed borosilicate framework is important for rational zeolite synthesis with controlled heteroatom siting, which has received considerable attention for many years. Such preferential B incorporation is supported by the DFT analyses, as summarized in Figure 6, which shows comparisons of experimental and calculated NMR data for different models of the $C_{16}H_{33}N^{+}$**Me$_2$Et**-directed borosilicate material, using reference candidate structures 2 (in a and b) and 3 (c, d), both shown in Supporting Information, Figure S5, and B atoms sitting in site Si1 (a, c) or Si2 (b, d). Data points corresponding to ^{29}Si Q^n sites are shown as open black circles in Figure 6, where they should be compared to the standard ^{29}Si 1D spectrum collected for this material, shown in black on top of the figure. Q^n(1B) ^{29}Si sites, represented as filled red squares, should be compared to the projection of the *J*-mediated HMQC spectrum, shown in red on top. Figure 6a is no more than a different representation of the data shown in Figure 4a-d, with B incorporated in Q^3 Si site Si1 within reference silicate framework structure 2 (see Figure S5), which shows in particular a very good agreement between experimental and calculated data for Q^n(1B) sites (red squares). A reasonably good agreement is also observed for Q^n(1B) in Figure 6c, when B is incorporated also in Q^3 Si site Si1, but within reference structure 3 instead of 2. By comparison, the models where the B is in substitution of Q^3 Si site Si2, as shown in Figure 6b,d, yield much poorer agreement between experiments and calculations. These results thus seem to establish that the preferential substitution site of the ^{11}B atoms in the $C_{16}H_{33}N^{+}$**Me$_2$Et**-directed layered borosilicate is Q^3 ^{29}Si site Si1.

2.g. Evaluations of $C_{16}H_{33}N^{+}Me_3$-directed borosilicate models: calculated NMR data vs. advanced experimental correlation NMR. The situation is remarkably different in the case of the $C_{16}H_{33}N^{+}$**Me$_3$**-directed borosilicate, where the incorporation of B atoms induces profound structural modifications of the silicate framework near B atoms, as was first evidenced by the three ^{11}B NMR signals (Figure 2b) that over specify the number of distinct ^{29}Si sites (only two in this case). To understand the local disorder near B species in the $C_{16}H_{33}N^{+}$**Me$_3$**-directed borosilicate materials, the same DFT-modeling approach using homogeneously-distributed positive charges instead of surfactant molecules was applied to calculate the ^{29}Si and ^{11}B NMR chemical shifts. Figure 7 shows two DFT-optimized models with the chemical composition $[BSi_{31}O_{64}(OH)_8]^{9-}$ that were obtained by substituting one B atom in Q^3 Si site Si1 (Figure 7a) or in Q^4 Si site Si2 (Figure 7d) in a 2x2x1 supercell. The main characteristics of these models are summarized in Table 4. The calculated NMR parameters based on these models are shown as vertical bars in the plots of Figure 7b,c,e,f. Calculated ^{29}Si chemical shifts are in reasonable agreement with the experimental data (black spectrum on top of Figure 7b, e) for both Q^3 and Q^4 ^{29}Si sites (black lines). Interestingly, the calculated ^{29}Si chemical shifts for Q^n(1B) ^{29}Si environments (blue lines in Figure 7b,e) exhibit small and non-systematic shift differences between Q^3(0B) and Q^3(1B) ^{29}Si or between Q^4(0B) and Q^4(1B) ^{29}Si sites. These DFT analyses suggest that, as in the case of the $C_{16}H_{33}N^{+}$**Me$_2$Et**-directed layered borosilicate, such Q^n(1B) ^{29}Si sites could be very hard to distinguish experimentally from Q^n ^{29}Si sites. As for ^{11}B chemical shifts, calculated values are significantly different for ^{11}B species inserted into a Q^3 or a Q^4 ^{29}Si site, as shown in Figure 7c and f, respectively, suggesting that ^{11}B site B1 (at -0.9 ppm) is very likely to correspond to the B species incorporated in the Q^3 Si site Si1 as a BOH moiety (Figure 7c). By comparison, ^{11}B signals at -1.9 and -2.5 ppm (labeled as ^{11}B sites B2 and B3, respectively) should be associated with the B atoms incorporated in the Q^4 Si site Si2 (Figure

7f). Nevertheless, these results do not explain the presence of two distinct four-coordinate ^{11}B sites B2 and B3, both of which are attributed to the B atoms at Q^4 environments in the $C_{16}H_{33}N^+$**Me$_3$**-directed borosilicate.

The challenges of understanding such complicated short-range disorder near ^{11}B species in borosilicate frameworks were again overcome by 2D *J*-mediated ^{11}B{^{29}Si} NMR techniques probing ^{11}B-O-^{29}Si site connectivities. Figure 8a shows the 2D ^2J(^{11}B-O-^{29}Si)-mediated HMQC ^{11}B{^{29}Si} NMR spectrum of *ca.* 99% ^{29}Si-enriched $C_{16}H_{33}N^+$**Me$_3$**-directed layered borosilicate materials, whose 1D ^{29}Si and ^{11}B NMR spectra are shown in black on right vertical and top horizontal axis of the 2D spectrum, respectively. The ^{29}Si projection shown in red on the right again selectively reflects a fraction of Q^n(1B) ^{29}Si environments that are not possible to identify via 1D ^{29}Si NMR analyses, because their ^{29}Si signals are obscured by the much larger fraction of ^{29}Si signals contributed by Q^n ^{29}Si environments. This ^{29}Si projection was included (in blue) in Figure 7b,e for direct comparison with calculated ^{29}Si chemical shifts corresponding to Q^n(1B) ^{29}Si environments, which reveal good agreements between the calculated and experimental results. Both experimental and theoretical NMR analyses indicate that framework B species have limited influences on their next-nearest-neighboring ^{29}Si sites.

Specifically, the ^{11}B signal at -2.5 ppm associated with ^{11}B site B3 exhibits in Figure 8a correlated intensities with the ^{29}Si signals at -111 and -101 ppm, corresponding to Q^4 and Q^3 ^{29}Si sites, respectively, establishing that the ^{11}B site B3 is bonded to the Q^3 and Q^4 ^{29}Si sites through bridging oxygen atoms. This is in agreement with the assignment of the ^{11}B site B3 inserted into Q^4 framework sites, because every Q^4 Si site is connected to two Q^3 and two Q^4 Si sites, as described using the DFT-optimized model shown in Figure 7a. On the contrary, ^{11}B signals B1 and B2 at -0.9 and -1.9 ppm, assigned to the B atoms incorporated into Q^3 and Q^4 Si environments, respectively, both show correlation intensities with the ^{29}Si signals

corresponding to Q^4 Si sites but no correlation with any ^{29}Si signals corresponding to Q^3 Si species. This is inconsistent with the site connectivities of either Q^3 or Q^4 ^{29}Si sites established from $C_{16}H_{33}N^+\mathbf{Me_3}$-directed silicate framework[71] and confirmed for the borosilicate (see SI, Fig. S1a). Indeed B atoms incorporated into Q^3 or Q^4 Si sites are expected to be bonded to one or two Q^3 Si atoms, respectively, which would lead to correlation intensities in the Q^3 ^{29}Si region (highlighted in Figure 8a). This analysis establishes that the local Si structure around B sites B1 and B2 is modified to have these B sites connected with Q^4 Si sites exclusively, reflecting a locally-increased degree of framework condensation with respect to the siliceous counterparts.

Such local structural rearrangements near B atoms in the $C_{16}H_{33}N^+\mathbf{Me_3}$-directed borosilicate material are supported via DFT calculations. For example, Figure 8b,c illustrates how a DFT-optimized borosilicate model (Fig. 8c) may be built using a supercell (in this case made of 1x3x1 cells of the reference pure-silicate structure, Figure 8b), where one Q^3 Si site was manually substituted by one B atom with the addition of a H to form a B-OH environment for charge compensation. The Q^3 Si atom bonded to the B site was manually connected with its next-nearest-neighbor Q^3 Si atom by replacing the two non-bridging oxygen atoms of these two Si atoms by a single bridging oxygen atom placed at their center of mass. In the example model shown here, the decreased framework charge caused by replacing two oxygen atoms with one oxygen atom was compensated by removal of two surfactant-mimicking $C_4H_9N^+\mathbf{Me_3}$ molecules, leading to a chemical composition $(BSi_{23}O_{53}H)^{10-} \cdot 10(C_4H_9N^+\mathbf{Me_3})$. Interestingly, this model appears to deform during the geometry optimization (Figure 8c) to accommodate the additional cross-linking between silicate units. This is a consequence of the local structural rearrangements necessary for SiO_4 and BO_4 units to retrieve appropriate tetrahedral geometries. The configurations of the B atoms inserted into Q^3 sites and their connected Si neighbors (Q^4(1B) only) in this model are

well consistent with all the experimental NMR data of the ^{11}B site B1. The ^{11}B chemical shift calculated via this model is 0.1 ppm, which is in reasonable agreement with the experimental ^{11}B shift of ^{11}B site B1 (-0.9 ppm). Similar results were obtained for other models describing the same situation yet with different supercell sizes or strategies for the compensation of framework negative charges, as summarized in Table S3. Collectively, they all yielded calculated ^{11}B shifts between 0.1 and -0.4 ppm, in similarly good agreement with the experimental ^{11}B peak at -0.9 ppm. As has been discussed above, however, the approach including surfactant-mimicking yields calculated ^{29}Si NMR data that are considerably more scattered than the experimental distributions of ^{29}Si chemical shifts.

Similar conclusions can be drawn for ^{11}B chemical shifts calculated with the alternative approach, where homogeneously distributed positive charges rather than surfactant molecules were applied for charge compensation in the surfactant-directed borosilicates, which are summarized in Table 4. For example, the DFT-optimized model with the chemical composition $[BSi_{31}O_{64}(OH)_7]^{8-}$ (Figure 9a) depicts a similar BOH environment in a 2x2x1 supercell with one ^{1}H atom per pair of non-bridging oxygen atoms. With this model, the calculated ^{11}B shift (0.2 ppm, see Figure 9c or Table 4) is very close to the calculated value using the surfactant-included models and in reasonable agreement with the ^{11}B signal associated with ^{11}B site B1. Calculations of ^{29}Si chemical shifts conducted under such conditions (Figure 9b) predict Q^4(1B) ^{29}Si signatures close to the region of the ^{29}Si spectrum correlated with the B1 frequency (Figure 8a), which is obscured by the dominant Q^4 ^{29}Si signal. In summary, all models that describe one ^{11}B atom inserted into Q^3 ^{29}Si site Si1 to form a B-OH and to induce a new Si-O-Si connectivity of its Q^3(1B) neighbor are compatible with the ^{11}B shift of ^{11}B site B1.

Similar calculations were conducted on various models that describe local structures of the ^{11}B site B2 (*i.e.* one ^{11}B atom incorporates into one Q^4 Si site), as well as its

connectivities with other Q^4 Si sites. Such local Si and B environments may be obtained by generating two additional framework condensations that involve the two Q^3 Si sites adjacent to the B atom, which become Q^4(1B) Si sites in the optimized structure. This procedure is illustrated in Figure S6 for the model of chemical composition $(BSi_{31}O_{70}H_6)^{7-}$ whose DFT-optimized structure in shown in Figure 9g. A very similar situation may alternatively be obtained incorporating B in a Q^3 Si site and transforming this B site to a Q^4 by creating a new B-O-Si connectivity with an adjacent Q^3 Si atom (thereby changed to a Q^4 Si). This and other models that describe the same type of Si and B environments, but with different initial locations of B atoms and charge-balance strategies (see Table 4) lead to ^{11}B chemical shifts between -3 and -4 ppm, which is not too far from the experimental ^{11}B shift of ^{11}B site B2 (-1.9 ppm). In combination with 2D NMR data, these calculations thus shed light onto the possible rearrangements of the framework topology (*i.e.*, the coordination sequences and ring structures) that may take place upon B incorporation into the $C_{16}H_{33}N^+$**Me$_3$**-directed layered borosilicate material during framework ordering. Such B incorporation appears to promote or to be facilitated by the condensation of originally incompletely-condensed Si atoms around the incorporated B site.

2.h. Understanding the differences between $C_{16}H_{33}N^+Me_2Et$- and $C_{16}H_{33}N^+Me_3$-directed borosilicate materials. When B atoms are incorporated into the two surfactant-directed silicate frameworks with very similar lamellar morphologies (see Section 2.a), prepared under identical synthesis conditions with very similar structure-directing alkylammonium molecules, profound differences appear between them. XRD and ^{11}B{^{1}H} correlation NMR data (section 2.c), along with ^{29}Si{^{1}H} correlation NMR data published previously for the siliceous analogs,[46] suggest that the orientations of the surfactant molecules and their interactions with silicate layers are similar in both materials. (In fact the latter appear to

primarily depend on the nature (Q3 or Q4) of the site in which the boron is incorporated.) We consequently believe that the origin(s) of the different boron sitting and distributions between these materials must be sought instead in the molecular structures of their layered frameworks. The presence of B atoms of smaller size as compared with Si atoms in a silicate framework with otherwise unchanged topology is expected to create certain amount of stress, which causes a relaxation of the bonding geometry to attain a stable conformation. This mechanism particularly depends on the availability of sufficient degrees of freedom, and the subtle differences between the molecular structures of the layered frameworks in the corresponding reference materials are important in this respect. For example, the $C_{16}H_{33}N^{+}$**Me$_2$Et**-directed silicates are slightly more condensed than the $C_{16}H_{33}N^{+}$**Me$_3$**-directed silicates, with 40% of Q^3 Si sites as compared to 50% for the other. This difference somehow contributes to imposing that the B atoms are located in a single T site that can accommodate such structural distortions more easily than others. The slightly more condensed $C_{16}H_{33}N^{+}$**Me$_2$Et**-directed frameworks, in particular, do not seem to allow for (or to necessitate) the additional cross-linking that occurs in some cases for the other borosilicate material. Another possible reason for such differences, which may also have impacts on the available degrees of freedom of the frameworks, is the different ways in which the linear chains formed by the Q^3 sites and their mutually H-bonded non-bridging oxygen atoms are arranged in the two different framework structures. These chains are aligned in the same direction above and below the plane in the $C_{16}H_{33}N^{+}$**Me$_2$Et**-directed materials, whereas the chains of Q^3 sites located on the top of a given layer are perpendicular to the ones located at the bottom in the $C_{16}H_{33}N^{+}$**Me$_3$**-directed materials. Possibly as a result of this difference, the lamellar structure of the $C_{16}H_{33}N^{+}$**Me$_2$Et**-directed material is less likely to deform such as to accommodate for new ^{29}Si-O-^{29}Si connectivities that appear to facilitate the incorporation of ^{11}B atoms into the framework of the $C_{16}H_{33}N^{+}$**Me$_3$**-directed materials.

It should be possible to relate these considerations to the differences in the amount of boron that can be incorporated in the two materials in identical synthesis conditions. All of our syntheses lead to a final amount of B (Si/B ~ *ca.* 50 to 140) that is considerably lower than used for the synthesis (Si/B = 2.5). And yet this final amount of B is generally higher for the $C_{16}H_{33}N^+$**Me$_2$Et**-directed materials, where the Si/B substitution can take place in a Q^3 Si site (a situation seemingly more favorable than in a Q^4 Si site) without local topological rearrangements of the framework. For the $C_{16}H_{33}N^+$**Me$_3$**-directed materials, one among the three distinct types of B sites that could be distinguished is still a Q^3 Si site, but we showed that its local Si environment is profoundly modified as compared to the Q^3 Si sites without covalently bonded to B atoms, with additional Si-O-Si connectivities involving the next-nearest neighbors of the boron. The topological rearrangements that promote (or are driven by) the B/Si substitution probably represent a relatively high energy barrier that makes this situation kinetically unfavorable. Another possible reason for the lower amount of boron incorporated in the $C_{16}H_{33}N^+$**Me$_3$**-directed materials is the shorter synthesis time (2 days) as compared to the $C_{16}H_{33}N^+$**Me$_2$Et**-directed material (7 days). These synthesis durations were kept to the minimum time needed to achieve a complete extent of molecular order in the reference silicate materials.[46] It is possible that longer crystallization times could lead to increased boron contents in the $C_{16}H_{33}N^+$**Me$_3$**- material, as previously reported by Zones and Hwang for borosilicate zeolite B-SSZ-42,[77] but this has not been extensively tested.

The astounding selectivity of B incorporation into a single type of Q^3 Si sites in the $C_{16}H_{33}N^+$**Me$_2$Et**-directed borosilicates cannot be explained by obvious thermodynamic criteria. As shown in Table 5, for a given framework (2 and 3 using the labeling of ref. 64) the energies calculated of models with B incorporated in site Si1 and Si2 are indeed very similar to each other (0.17 and 0.02 eV difference for frameworks 2 and 3, respectively). The accessibility to both Q^3 sites being seemingly the same (both correspond to the most easily-

accessed parts on the top and bottom of each layer, as shown in Figure S5), one can therefore think of reasons related to differences in the local structure around these sites. For example, analyses of the average T-O-T angles around Si sites Si1 and Si2 in the reference frameworks without B incorporation (Table 5) indicate significantly lower angle values around site Si1 as compared to Si2. In addition, the average B-O-Si angle appears to be systematically lower than the corresponding average Si-O-Si angle of the considered substitution Si site in the reference silicate model, as expressed in Table 5 by the negative values of their difference Δ. This suggests that the smaller average T-O-T angle around Si1 might correspond to a lower energy barrier for the incorporation of B in this site as compared to the other Q^3 Si site Si2 because the structural rearrangements required to accommodate the B atom are less pronounced in substitution of a site Si1. This explanation is compatible with the low amount of B that can be incorporated into the $C_{16}H_{33}N^+$**Me$_2$Et**-directed silicate frameworks, which indicates a relatively high energy barrier during the synthesis, and thus a kinetically-limited process.

Conclusions

We have established the B site distributions in the two chemically and structurally related $C_{16}H_{33}N^+$**Me$_3$**- and $C_{16}H_{33}N^+$**Me$_2$Et**-directed layered borosilicates by using advanced solid-state NMR techniques, in conjunction with DFT calculations. The results and analyses reveal that B atoms are incorporated into different types of framework sites in the $C_{16}H_{33}N^+$**Me$_3$**-directed borosilicates, and induce in some cases local topological rearrangements of nearby Si sites that tend to be more polymerized than in the reference silicate framework. In $C_{16}H_{33}N^+$**Me$_2$Et**-directed borosilicates, in contrast, B atoms are shown to be selectively incorporated into one type of Q^3 ^{29}Si sites without topological modifications of the framework. Furthermore, the distorted local environments near B sites in $C_{16}H_{33}N^+$**Me$_2$Et**-directed borosilicates appear similar throughout the framework, resulting in

a degree of molecular order that approaches that of crystalline structures, though without long-range periodicity. The ability of NMR combined with DFT calculations to distinguish between topological and subtle geometrical disorder resulting from a chemical disorder in otherwise molecularly-ordered solids may be a key to understand the origins of many advanced materials properties.[23] In particular, the types and distributions of order and disorder near framework B sites in the borosilicate frameworks studied here might well be correlated with the reaction and other material properties of borosilicates, as is now well-established for aluminosilicate zeolites.[12] While there is little evidence that this is also true for borosilicates, which have received less attention, some studies nevertheless revealed different conversion rates and selectivities of borosilicate zeolites depending on the Si/B ratios,[78] which may be interpreted as changes in the B sitting among the different framework sites as the B content changes. The molecular-level insights into B site distributions in the two surfactant-directed borosilicates are expected to guide rational syntheses of borosilicate zeolite catalysts with controlled B site distributions.

Materials and Methods

Materials Syntheses Cetyltrimethylammonium bromide ($C_{16}H_{33}$**Me$_3$**NBr, ≥96.0%, Sigma-Aldrich), cetyldimethylethylammonium bromide ($C_{16}H_{33}$**Me$_2$Et**NBr, ≥98%, Sigma-Aldrich), tetramethylammonium hydroxide (TMAOH, 25 wt% in water, Sigma-Aldrich), boric acid (Sigma-Aldrich), hydrofluoric acid (HF, 48 wt% in water, Sigma-Aldrich), nitric acid (HNO_3, ACS reagent and 70%), amorphous silica (SiO_2, CAB-O-SIL M5 scintillation grade, ACROS ORGANICS) and methanol (ACS grade, VWR®) were purchased and directly used without any further purification. 99% ^{29}Si-enriched SiO_2 was purchased from CortecNet (France). Syntheses of layered surfactant-directed borosilicates follow the molar composition of 1.0 SiO_2: 0.2 B_2O_3: 0.7 TMAOH: 113.4 H_2O: 9.9 CH_3OH: 0.7 surfactants (either $C_{16}H_{33}Me_3NBr$

or $C_{16}H_{33}Me_2EtNBr$). Surfactants were dissolved in deionized water. TMAOH and CH_3OH were subsequently added and the solution stirred for 30 min, after which silica precursors (either SiO_2 or recondensed $^{29}SiO_2$) were added, and the reaction media stirred for a week. Boric acid was then added for 2 h to obtain synthesis gels, which were transferred into a Teflon™-lined Parr™ 4745 stainless-steel reactor, well-sealed and heated at 135 °C under static conditions for 2 ($C_{16}H_{33}N^+$**Me$_3$**-directed borosilicates) and 7 days ($C_{16}H_{33}N^+$**Me$_2$Et**-directed borosilicates). These crystallization times correspond to the minimal duration needed to obtain complete extents of molecular order for the corresponding reference silicate structures of both materials.[46] After the hydrothermal treatment, the as-synthesized layered surfactant-directed borosilicates were collected using vacuum filtration and washed with deionized water. The products were dried at 90 °C overnight before characterization.

Recondensed $^{29}SiO_2$ was prepared by dissolving ^{29}Si-enriched SiO_2 in 1M TMAOH solution (pH ~ 14) under reflux 95 °C and stirring conditions for 19 days. The ^{29}Si-enriched silica was subsequently recovered by adding concentrated HBr acid solution to obtain precipitate gels (pH of 7 - 8), which were subsequently collected by vacuum filtration. The precipitated gels were purified by deionized water, high-speed centrifugation, and removal of excess water. The purified silica source (designated as recondensed $^{29}SiO_2$) was dried at 90 °C for several days prior to syntheses of borosilicates.

Elemental analyses. Bulk Si/B ratios were obtained using inductively coupled plasma (ICP) analysis (Thermo iCAP 6300 model). Before ICP analysis, the as-synthesized layered materials were calcined at 550 °C for 12 h to remove organic surfactants, and the resulting calcined materials were dissolved with 2 wt% HF and 3 wt% HNO_3 acid solution under vigorous stirring conditions for several days. The CHN results were provided by the analytical lab in the Marine Science Institute (MSI), UCSB using the CEC440HA model from Exeter Analytical, Inc.

Solid-state NMR. Solid-state one-dimensional (1D) ^{11}B, ^{29}Si and two-dimensional (2D) ^{11}B{^{1}H} HETCOR NMR experiments were performed on a Bruker Avance (III) 750 and 400 NMR spectrometers operating at 17.6 (^{1}H, ^{11}B, and ^{29}Si Larmor frequencies of 750.12, 240.66, and 149.01 MHz, respectively) and 9.4 T (^{1}H, ^{11}B, and ^{29}Si frequencies of 400.17, 128.38, and 79.49 MHz, respectively). The 1D ^{29}Si{^{1}H} CP-MAS experiments were collected at room temperature, at 17.6 T and at 10 kHz under conditions of magic angle spinning (MAS) using a 4 mm probehead, with a cross-polarization (CP) contact time of 8 ms and a recycle delay of 2 s, with 4k transients for the natural abundance sample and 128 scans for the ^{29}Si enriched sample. ^{11}B echo-MAS experiments were performed at 17.6 T, at the MAS frequency of 14 kHz using recycling delay of 2 s, with double frequency sweep (DFS)[79] preparation sequence to increase signal. Heteronuclear ^{1}H decoupling at a nutation frequency of 50 kHz with SPINAL64[80] was utilized during acquisition for both ^{29}Si and ^{11}B NMR experiments. Transverse dephasing time measurements were performed with 7 increments to obtain a series of half-echo delays between 0 and 12 ms, each collected with 1024 scans. Heteronuclear ^{1}H decoupling (SPINAL64) at a nutation frequency of 60 kHz alternatively turned on and off during the echo (and kept on during the acquisition).

Two-dimensional (2D) ^{11}B{^{1}H} HETCOR NMR spectra were collected at room temperature at 17.6 T and under MAS conditions of 14 kHz using a 4 mm probehead. The magnetization was transferred from ^{1}H to ^{11}B by using adiabatic passage through Hartmann-Hahn condition.[81] CP contact time of 1 and 0.1 ms were used for the $C_{16}H_{33}N^{+}Me_3$- and $C_{16}H_{33}N^{+}Me_2Et$-directed layered borosilicates, respectively. The signal in the 2D ^{1}H dimension was accumulated over 96 increments with 176 transients each for the $C_{16}H_{33}N^{+}Me_3$-directed material and 128 increments with 64 transients each for the $C_{16}H_{33}N^{+}Me_2Et$-directed material. Heteronuclear ^{1}H decoupling at a nutation frequency of 70

kHz was applied during acquisition. Both spectra were collected using a repetition delay of 2 s.

Two-dimensional $^{11}B\{^{29}Si\}$ dipolar- and *J*-mediated HMQC spectra were collected at 9.4 T on materials synthesized with ^{29}Si enrichment, at a MAS frequency of 10 kHz (using 3.2 mm triple-resonance probehead). The heteronuclear dipolar couplings between ^{11}B and ^{29}Si species were reintroduced in dipolar-mediated $^{11}B\{^{29}Si\}$ HMQC by means of a $R4^2_1$ symmetry-based dipolar recoupling[82-85] scheme at a ^{29}Si nutation frequency of 20 kHz ($2\nu_R$). The recoupling durations were set to 6 ms (10 symmetry cycles of 6 rotor periods each) before and after the evolution period. The second ^{29}Si dimension was collected with 96 increments, with 1024 transients each, and a repetition delay of 2.17 sec (total experimental duration of 61 hours). The half-echo delay before and after the evolution period in the $^{11}B\{^{29}Si\}$ *J*-mediated HMQC[86] experiments were optimized experimentally to 10 and 12.5 ms for the $C_{16}H_{33}N^+$**Me$_3$**- and $C_{16}H_{33}N^+$**Me$_2$Et**- directed layered borosilicates, respectively. The indirect dimensions were collected with 32 increments (2304 scans each) for the former material and 96 increments for the latter (768 transients each). Recycling delays of 3 second for both materials led to experimental durations of 62 and 63 hours, respectively. Heteronuclear ^1H decoupling with the SPINAL64 sequence at a nutation frequency of ca. 60 kHz was applied during the whole sequence. NMR ^{29}Si and ^{11}B chemical shifts were referenced to tetra methyl silane (TMS) and BF_3OEt_2, respectively.

Error calculations for the transverse dephasing time measurements were conducted with a Monte Carlo approach, by repeating the same fit on 512 sets of data points generated by adding random noise to the experimental data set added. The standard deviation of the added random noise was fixed to the standard deviation between the experimental points and the best fit. The reported errors correspond to the standard deviation of the fitted data over the 512 fits.

X-ray diffraction. The mesostructures and local periodic orderings were characterized using small-angle (SAXS) and wide-angle (WAXS) X-ray diffractions. SAXS patterns were collected using a Riguku SMART lab diffractometer and a Cu Kα radiation (λ = 1.5405 Å) generated at 44 kV and 40 mA. The scanning angle range of a SAXS pattern was from 0.5 to 10° 2θ and the step size was set to 0.5 °/min. Furthermore, WAXS patterns were collected using a Philips XPERT Pro diffractometer and a Cu Kα radiation (λ = 1.5405 Å) generated at 45 kV and 40 mA. The materials were scanned at a step size of 4 °/min between 2θ angle ranges from 10 to 45°.

DFT Calculations. DFT Calculations were conducted with CASTEP,[87] a code based on Density Functional Theory that uses a plane-wave approach and periodic boundary conditions. Geometry optimizations were conducted using PBE as an exchange correlation functional,[88] a cut-off energy of 650 eV, and the default "on-the-fly" "ultrasoft" pseudopotentials[89] of Materials Studio (see pseudopotential details in Supporting Information, Table S4) with convergence thresholds of 10^{-5} eV/atom for the total energy, $3x10^{-2}$ eV/Å for the maximum ionic force, and 10^{-3} Å for the maximum ionic displacement. During the geometry optimization, unit cells were kept frozen, while all the atoms inside were allowed to relax in order to minimize both the forces on the atoms and on the unit cell. Depending on the model size, different Monkhorst-Pack[90] (MP) grid was used to sample the Brillouin zone so as to give a k-spacing less than 0.04 $Å^{-1}$ in the *a*, *b*, *c* directions. For example, a 4×4×1 MP grid is used when calculation was made on one unit cell (10 or 8 Si atoms depending on the material), whereas MP grids of size 4×2×1, 2×4×1, 2×2×1, and 3×1×1 were used for the 1×2×1, 2×1×1, 2×2×1, and 1×3×1 supercells, respectively.

Calculations of NMR shielding values were performed using the Gauge Including Projector Augmented Wave approach[91] (GIPAW) method implemented in CASTEP using the same conditions for cut-off energy and MP grid as for geometry optimizations. Reliable

absolute chemical shift values may be obtained from correlation plots between experimental isotropic chemical shifts and calculated isotropic chemical shielding for an appropriate series of reference compounds in order to cover a large domain of chemical shifts for each type of nuclei. Here, we used for ^{29}Si and ^{11}B chemical shifts calculations the compounds listed in Table S3 (Supporting information), which gave rise to the correlation plots shown in Figure S7 (Supporting information). The correlation equations were respectively: δ_{iso}(ppm) = *-0.920* σ_{iso} + *288.45* for ^{29}Si, and δ_{iso}(ppm) = *-1.004* σ_{iso} + *95.31* for ^{11}B.

ACKNOWLEDGEMENTS

This work was supported by an international collaborative grant between the U.S. National Science Foundation (NSF) (CHE-0924654) and the French ANR (ANR-09-BLAN-0383-CSD 3 "ALUBOROSIL"). Portions of this work were carried out using the Central Facilities of the UCSB Materials Research Laboratory supported by the MRSEC Program of the U.S. NSF under award DMR-1121053; the MRL Central Facilities are a member of the NSF-funded Materials Research Facilities Network (www.mrfn.org). For DFT calculations, we thank the "Centre de Calcul Scientifique en region Centre" (Orléans, France), CINES for access to the supercomputer JADE (Project # c2011096604), and the French ANR (ANR-11-MONU-003 "ExaviZ") for funding.

SUPPORTING INFORMATION PARAGRAPH

Two-dimensional through-bond-mediated ^{29}Si-^{29}Si correlation spectra (Figure S1) Estimations of the range of the perturbation induced by B incorporation (Table S1). Transverse dephasing time measurements (Figure S2). Model borosilicate structures using surfactant-mimicking alkylammonium molecules for the charge balance (Figure S3). Comparisons between experimental and calculated ^{29}Si chemical shifts (Figure S4). Summary

of ^{11}B chemical shift calculations conducted for models of the $C_{16}H_{33}N^{+}$**Me$_3$**- and $C_{16}H_{33}N^{+}$**Me$_2$Et**- directed borosilicates with surfactant-mimicking molecules (Table S2 and S3, respectively). DFT-optimized models of the reference $C_{16}H_{33}N^{+}$**Me$_2$Et**-directed silicate material and corresponding calculations of ^{29}Si chemical shifts (Figure S5). Illustration of the procedure used to build a borosilicate model with two additional Si-O-Si connectivities (Figure S6). Description of pseudo-potentials used in DFT calculations (Table S4). Calculated shielding and experimental chemical shifts of reference compounds of known crystal structure (Table S5). Correlation plots between experimental chemical shifts and calculated shielding (^{11}B and ^{29}Si) of known structure (Figure S7).

TABLES.

Table 1. Elemental analyses of $C_{16}H_{33}N^+Me_2Et$- and $C_{16}H_{33}Me_3N^+$-directed layered borosilicates (samples with natural ^{29}Si abundance).

Material	Atom content (wt%)					Si/B	surfactant per Q^3 unit
	C	H	N	Si	B		
$C_{16}H_{33}N^+\mathbf{Me_3}$ - borosilicate	37.5	7.4	2.5	18.4	0.05	142	0.64
$C_{16}H_{33}N^+\mathbf{Me_2Et}$ - borosilicates	42.1	7.4	2.7	17.7	0.13	52	0.71

Table 2. Transverse ^{11}B dephasing times (T_2') measured for $C_{16}H_{33}N^+Me_2Et$- (Si/B ~52) and $C_{16}H_{33}N^+Me_3$-directed layered borosilicates (Si/B ~142) with and without heteronuclear ^1H decoupling during ^{11}B signal acquisition.

Material	^{11}B peak position (ppm)	T_2' (ms)		^{11}B assignment
		decoupling on	decoupling off	
$C_{16}H_{33}N^+\mathbf{Me_2Et}$ - layered borosilicate	-0.4	35 ± 4	3.7 ± 0.2	hydroxylated
$C_{16}H_{33}N^+\mathbf{Me_3}$ - layered borosilicate	-0.9	24 ± 1	6.7 ± 0.4	hydroxylated
	-1.9	24 ± 7	16 ± 2	fully condensed

Table 3. Experimental and DFT ^{11}B chemical shift values for $C_{16}H_{33}N^+Me_2Et$-directed layered borosilicates based on the siliceous counterparts (Frameworks 2 and 3), where surfactants have been replaced by homogeneously-distributed positive charges for charge compensation.

Model composition and charge	B/Si substitution site	Calculated $\delta_{iso}(^{11}B)$ (ppm)		Experimental ^{11}B shift (ppm) [a]
		Framework 2	Framework 3	
$[BSi_{39}O_{80}(OH)_8]^{9-}$	Si1(Q^3)	0.3	0.9	-0.4
	Si2(Q^3)	-0.8	0.5	
	Si3(Q^4)	-2.8	-2.8	
	Si4(Q^4)	-3.8	-3.2	
	Si5(Q^4)	-3.9	-4.1	

Table 4. ^{11}B chemical shift values calculated by DFT for the model structures of the $C_{16}H_{33}N^{+}Me_3$-layered borosilicate material with surfactants replaced by homogeneously-distributed positive charges and 2×2×1 supercells.

Model composition and charge	B/Si substitution site	New framework connectivity	BOH/SiOH groups	Calculated $\delta_{iso}(^{11}B)$ (ppm)	Experimental ^{11}B shift (ppm)[a]
$[BSi_{31}O_{64}(OH)_8]^{9-}$	Si1(Q^3) as BOH	None	1 BOH / 7 SiOH	-0.2	-0.9
$[BSi_{31}O_{64}(OH)_8]^{9-}$	Si2(Q^4)	None	8 SiOH	-3.4	-2.5
Models with additional Si-O-Si or Si-O-B connectivities.					
$[BSi_{31}O_{64}(OH)_7]^{8-}$	Si1(Q^3) as BOH	1 Si-O-Si	1 BOH / 6 SiOH	0.2	-0.9
$[BSi_{31}O_{64}(OH)_7]^{8-}$	Si1(Q^3 => Q^4)	1 Si-O-B	7 SiOH	N.A.[c]	
$[BSi_{31}O_{64}(OH)_7]^{8-}$	Si2(Q^4)	1 Si-O-Si	7 SiOH	-3.5	-2.5
$[BSi_{31}O_{64}(OH)_6]^{7-}$	Si2(Q^4)	2 Si-O-Si	6 SiOH	-3.0	-1.9

[a] The ^{11}B experimental shift corresponds to the position of the experimental peak that gives the best match between all available experimental and calculation constraints.
[b] depending on the position of the additional Si-O-Si connectivity.
[c] The additional Si-O-B connectivity formed (manually) on the starting structure broke in the course of the optimization to form a three-coordinated BO_3 environment. No such environment was observed by ^{11}B NMR (Figure 2b) and this model was consequently discarded.

Table 5. Local structure analyzes around (potential) B incorporation site in the reference silicate and borosilicate framework models of the $C_{16}H_{33}N^{+}$**Me$_2$Et-**directed material**.**

Model composition	Reference framework	B incorporation site	Energy (eV)	Average T-O-T Angle		
				Name	Value (°)	Δ (°) [a]
$[Si_{10}O_{20}(OH)_2]^{2-}$	2		-11436.09	Si1-O-Si	143.5	
				Si2-O-Si	151.8	
	3		-11435.99	Si1-O-Si	144.6	
				Si2-O-Si	151.8	
$[BSi_{39}O_{80}(OH)_8]^{8-}$	2	Si1	-45652.59	B-O-Si	138.8	-4.7
		Si2	-45652.46	B-O-Si	150.1	-1.7
	3	Si1	-45652.10	B-O-Si	138.8	-5.8
		Si2	-45652.08	B-O-Si	140.7	-11.0

[a] Δ is the difference between the average B-O-Si angle and the corresponding average Si-O-Si angle in the reference structure (without B incorporation).

FIGURES AND CAPTIONS.

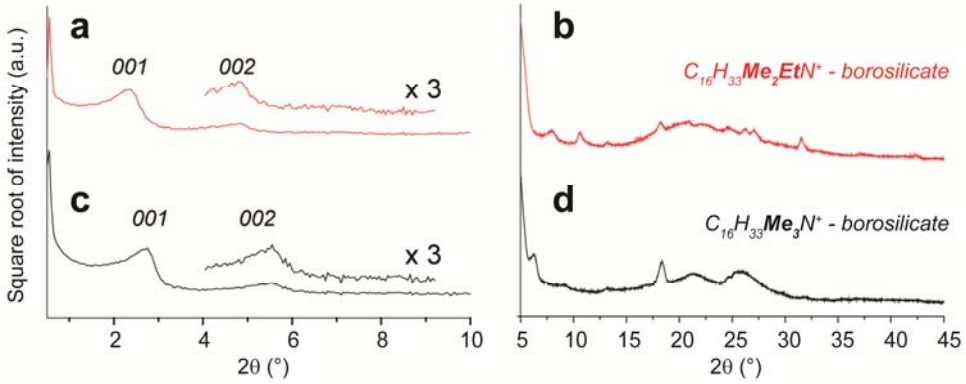

Figure 1. (a,c) Small- and (b, d) wide-angle powder X-ray diffraction patterns of as-synthesized (a,b) $C_{16}H_{33}N^+$**Me_2Et-** (Si/B ~52) and (c,d) $C_{16}H_{33}N^+$**Me_3-**directed layered borosilicates (Si/B ~142) with natural ^{29}Si abundance.

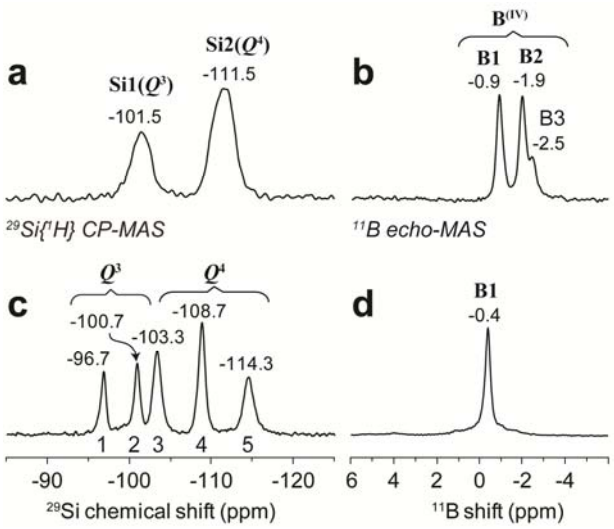

Figure 2. Solid-state 1D (left) $^{29}Si\{^{1}H\}$ CP-MAS and (right) ^{11}B echo-MAS NMR spectra of (a-b) $C_{16}H_{33}N^{+}$**Me$_3$**- (Si/B ~142) and (c-d) $C_{16}H_{33}N^{+}$**Me$_2$Et**-directed layered borosilicates (Si/B ~52), respectively. The spectra were all collected at 17.6 T and room temperature. Distinct ^{29}Si and ^{11}B species with their corresponding chemical shifts are described in detail in each MAS NMR spectrum.

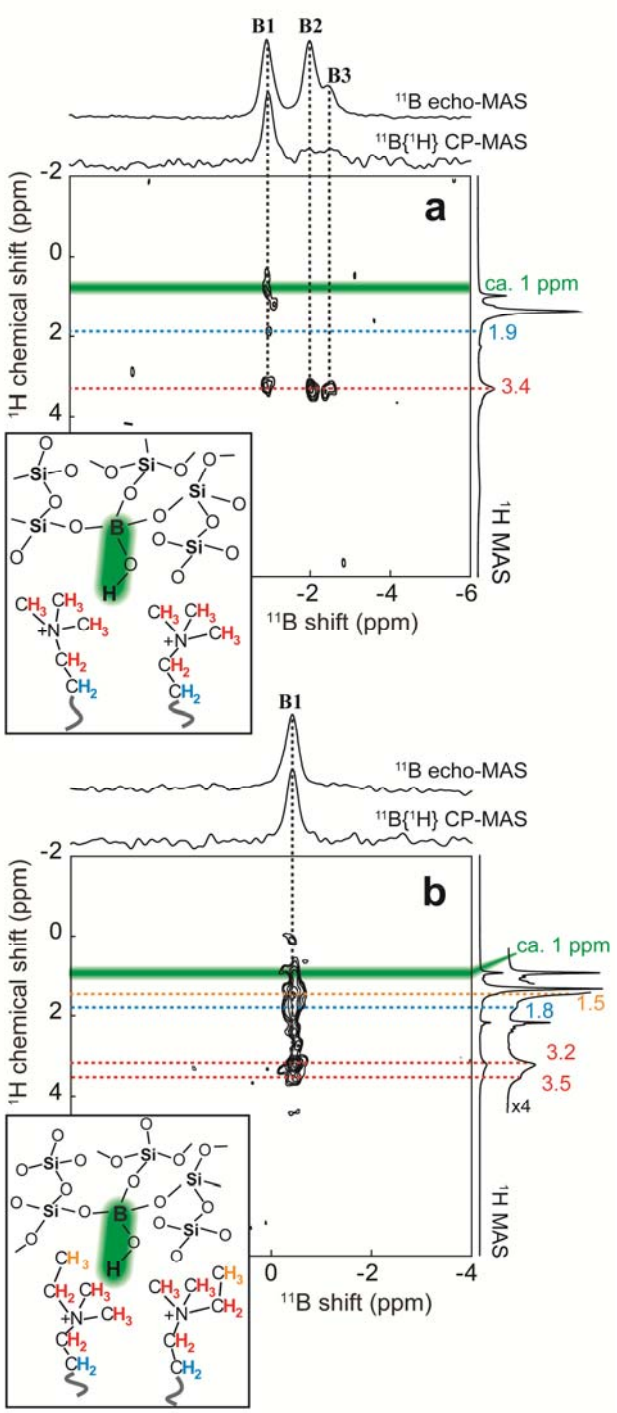

Figure 3. Solid-state 2D HETCOR ^{11}B{^{1}H} NMR spectra, acquired at 17.6 T and room temperature, of (a) $C_{16}H_{33}N^{+}$**Me$_3$**- (Si/B ~142) and (b) $C_{16}H_{33}N^{+}$**Me$_2$Et**-directed layered borosilicates (Si/B ~52), establishing spatial proximities between the four-coordinate ^{11}B and their nearby ^{1}H species. The corresponding 1D ^{11}B echo-MAS and ^{11}B{^{1}H} CP-MAS NMR spectra are shown along the top horizontal axis, and the 1D ^{1}H MAS spectrum is shown along the right vertical axis. The horizontal lines in different colors point to the various ^{1}H environments of the surfactants, as illustrated as insets.

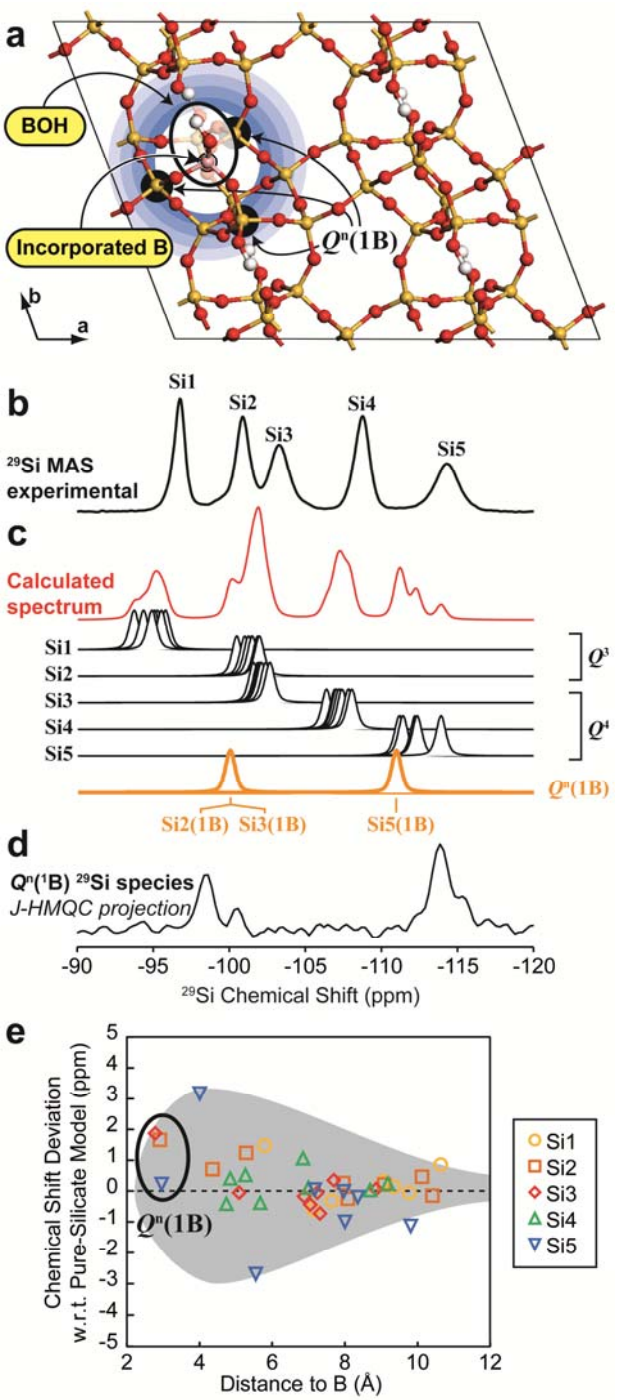

Figure 4. (a) DFT-optimized structural model of $C_4H_9N^+$**Me$_2$Et**-directed layered borosilicates with one ^{11}B atom inserted into one ^{29}Si site 1 (Q^3 ^{29}Si), which was constructed using a 2x2x1 supercell and has 8 ^{1}H atoms as well as homogenously distributed positive charges for charge compensation. (b) The 1D ^{29}Si NMR MAS spectrum of $C_{16}H_{33}$**Me$_2$Et**N^+-directed layered borosilicates (Si/B ~52) is comparison with (c) the calculated ^{29}Si NMR spectrum (in red) via DFT calculation that includes ^{29}Si signals corresponding to distinct types of Q^n (in black) and Q^n(1B) ^{29}Si species (in orange). (d) The 1D ^{29}Si projection extracted from 2D *J*-mediated HMQC ^{11}B{^{29}Si} NMR spectrum shows ^{29}Si signals associated with Q^n(1B) ^{29}Si sites. (e) A summary plot manifests differences of calculated ^{29}Si chemical shifts between the borosilicate model and the silicate model (*i.e.*, no ^{11}B

incorporation) as a function of relative distances of various ^{29}Si sites with respect to the nearest ^{11}B atoms. The influences of ^{11}B atoms on borosilicate frameworks are depicted in grey for visual illustrations.

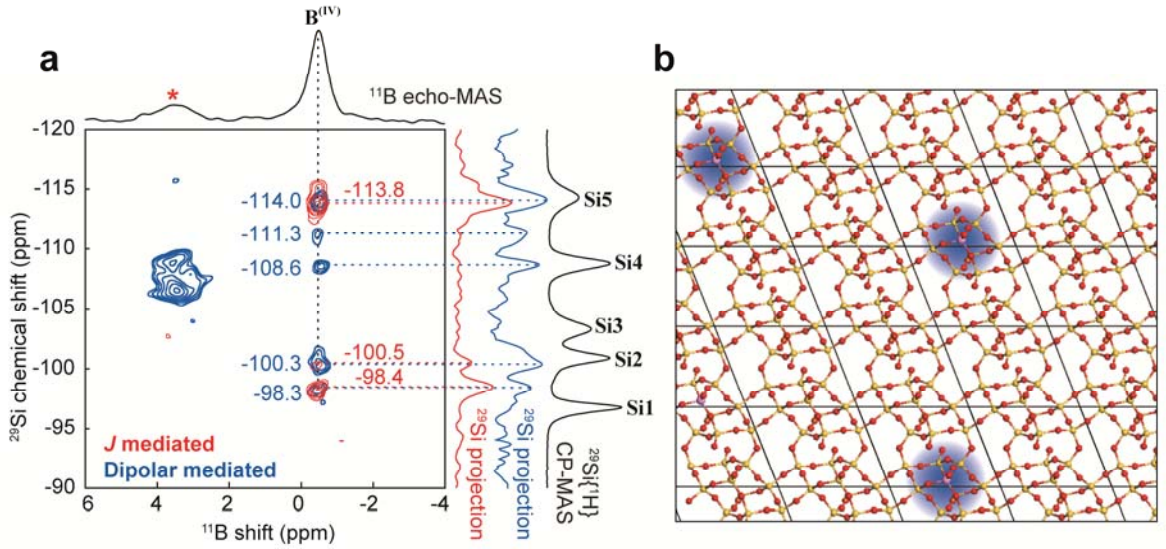

Figure 5. (a) Solid-state 2D dipolar- (in blue) and *J*-mediated (in red) HMQC ^{11}B{^{29}Si} NMR spectra, acquired at 9.4 T and room temperature, of ^{29}Si-enriched $C_{16}H_{33}N^{+}$**Me$_2$Et**-directed layered borosilicates (Si/B ~52 expected), which establish spatial proximities and site connectivities between ^{29}Si and ^{11}B species, respectively. The 1D ^{11}B echo-MAS spectrum is shown along the top horizontal axis. The ^{29}Si{^{1}H} CP-MAS spectrum (in black) and the ^{29}Si projections, extracted from 2D dipolar- (in blue) and *J*-mediated (in red) ^{11}B{^{29}Si} NMR spectra that focus on the regions associated with $C_{16}H_{33}N^{+}$**Me$_2$Et**-directed layered borosilicates (*i.e.*, from 1.0 to -2.0 ppm in the ^{11}B dimension), are all shown along with the right vertical axis. (b) A schematic representation illustrates the ^{11}B atom distributions in $C_{16}H_{33}N^{+}$**Me$_2$Et**-directed layered borosilicates, where the influences of ^{11}B sites on borosilicate frameworks are highlighted in blue.

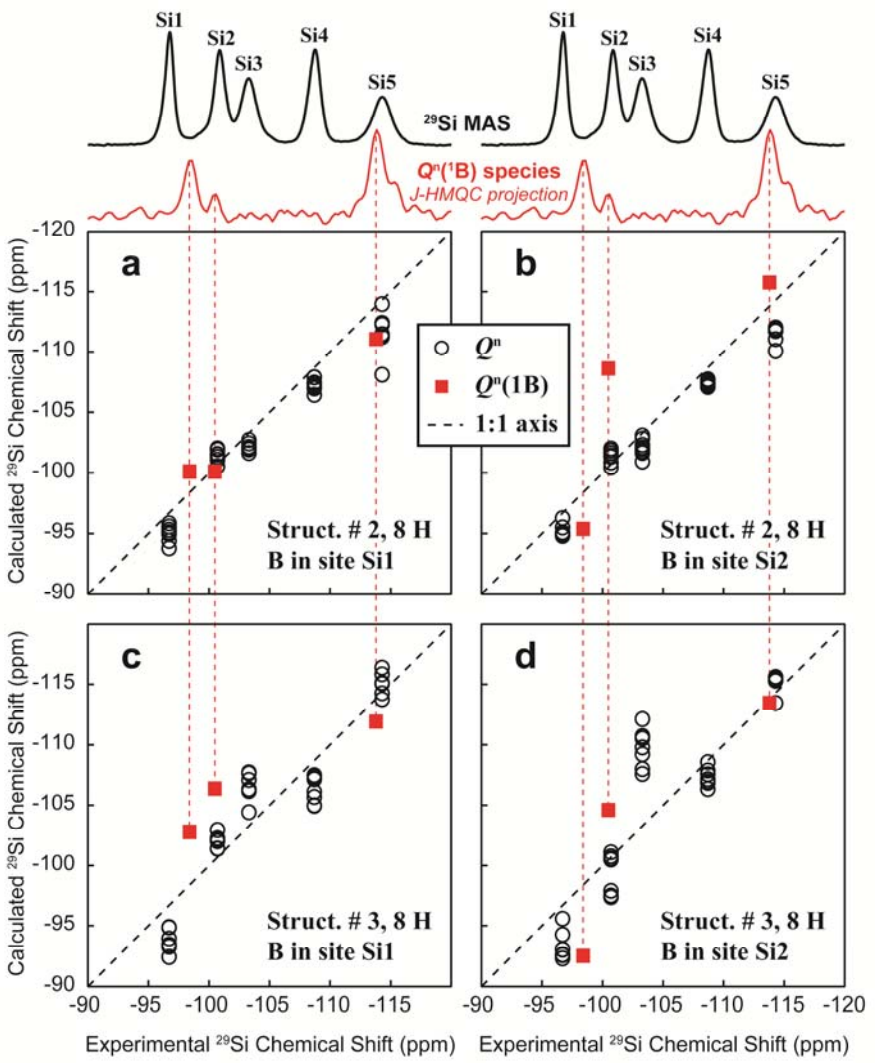

Figure 6. Comparisons between experimental and calculated ^{29}Si chemical shifts for 4 distinct DFT-optimized models of the $C_{16}H_{33}N^{+}$**Me$_2$Et**-directed borosilicate material. All structures were obtained from pure-silicate structures # 2 and 3 (see Figure S5), by considering a 2×2×1 supercell and replacing one Q^3 Si atom (site Si1 or Si2) by a B atom. Surfactants are omitted in these models and simply replaced by positive charges homogeneously distributed across the entire supercell. Black circles and red squares correspond to the ^{29}Si chemical shifts of Q^n and Q^n(1B) sites, respectively. Experimental ^{29}Si chemical shift values for Q^n(1B) sites are obtained from the projection of the *J*-mediated ^{11}B-^{29}Si correlation NMR spectrum (shown in red above the plots), which selectively reveals ^{29}Si sites connected (via a bridging O atom) to a B atom. The positions of the red squares are derived from the assignment giving the best agreement between experimental and calculated ^{29}Si chemical shifts for these sites.

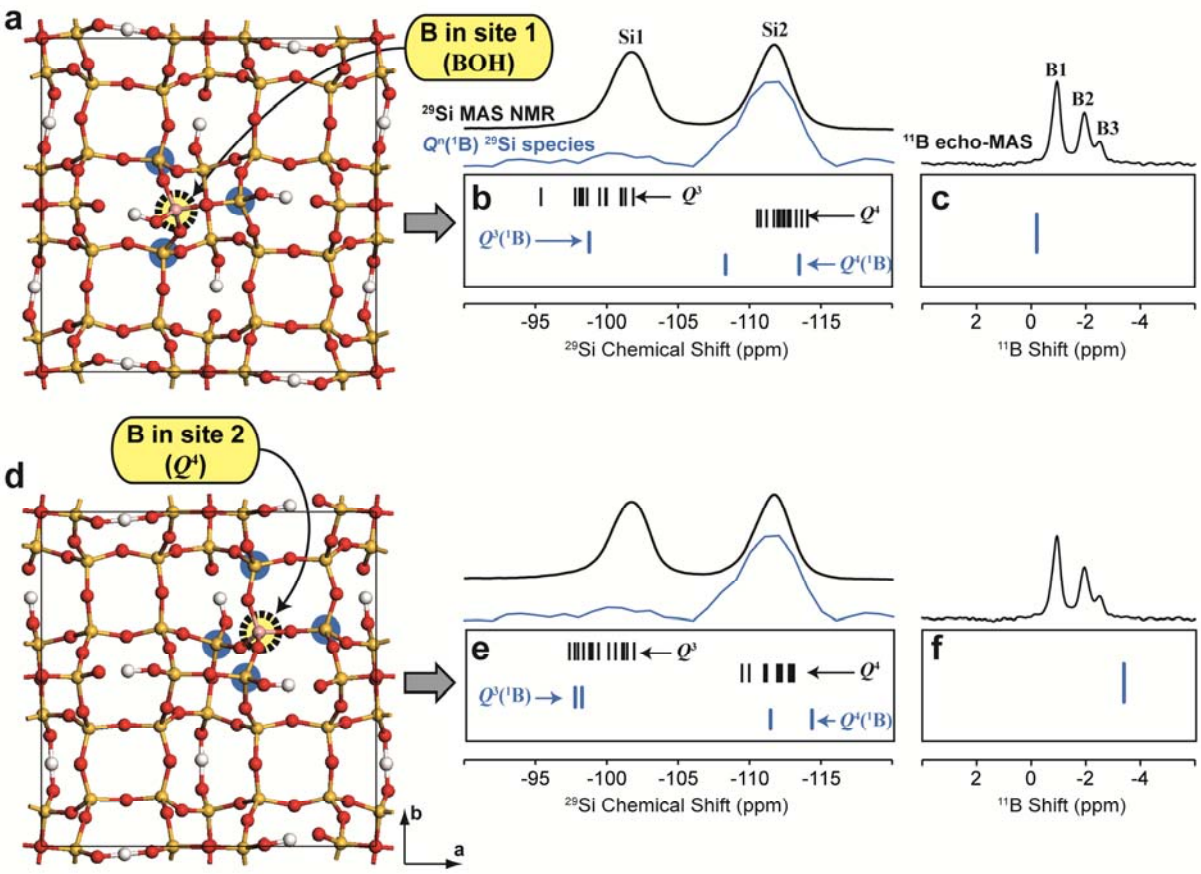

Figure 7. DFT-optimized structural models of $C_{16}H_{33}N^+$**Me$_3$**-directed layered borosilicates viewed from the c-axis, where ^{11}B atoms are manually inserted into ^{29}Si site (a) Si1 or (d) Si2. For each structural model, 8 ^{1}H atoms per unit cell and other homogeneously distributed positive charges are included for charge compensation. Calculated isotropic chemical shifts for distinct ^{29}Si and ^{11}B species in the models (a) and (b) are shown in plots (b, c) and (e, f), respectively, where the ^{29}Si chemical shifts in blue reveal the ^{29}Si species connected to one ^{11}B atom only. Experimental ^{29}Si and ^{11}B MAS NMR spectra are shown along the top axis accordingly for reference.

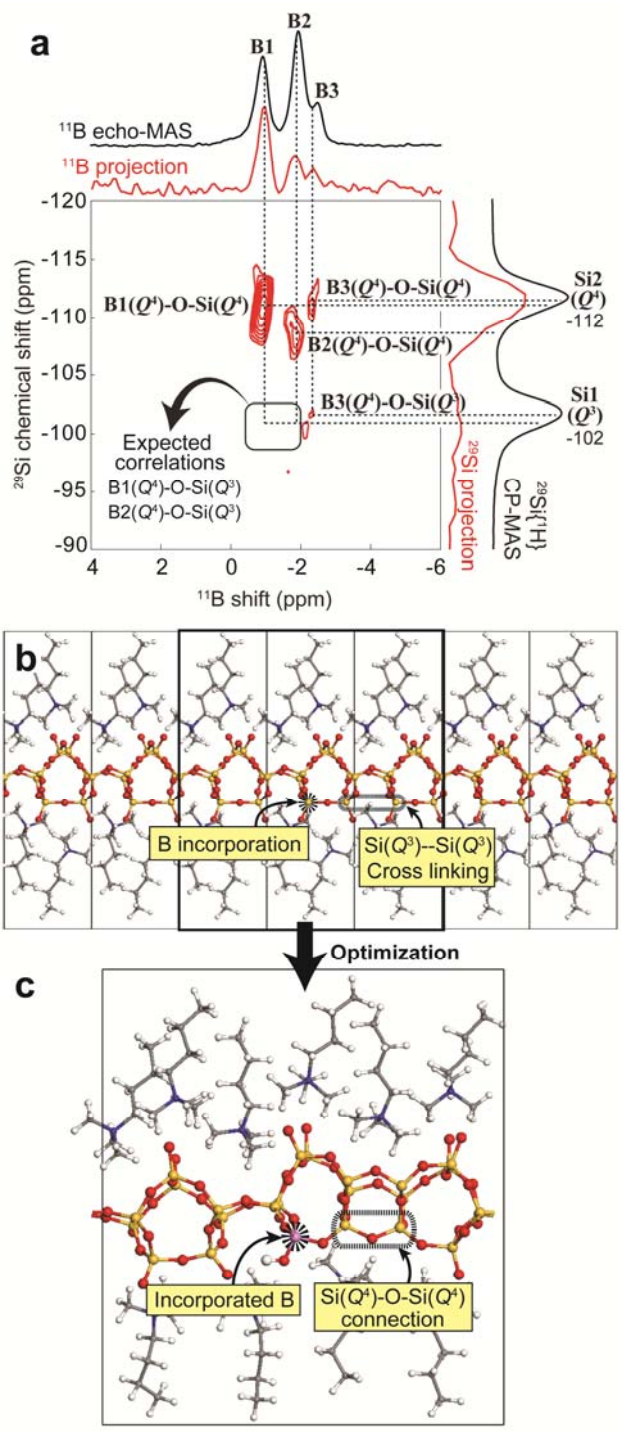

Figure 8. (a) Solid-state 2D *J*-mediated HMQC ^{11}B{^{29}Si} NMR spectrum, acquired at 9.4T and room temperature, of ^{29}Si-enriched $C_{16}H_{33}N^+$**Me$_3$**-directed layered borosilicates (Si/B ~142 expected), establishing ^{29}Si-O-^{11}B site connectivities between the ^{11}B species and their next-nearest-neighboring ^{29}Si sites through bridging oxygen atoms. The 1D ^{11}B echo-MAS NMR spectrum (in black) and the ^{11}B projection (in red) are shown along the top horizontal axis. The 1D ^{29}Si{^{1}H} CP-MAS spectrum (in black) and the ^{29}Si projection (in red) are shown along the right vertical axis. (b) The structural model of $C_{16}H_{33}N^+$**Me$_3$**-directed borosilicates for DFT optimization was constructed using multiple unit cells. (c) An example is selected to illustrate local structural changes in the DFT-optimized model of $C_{16}H_{33}N^+$**Me$_3$**-

directed borosilicates per supercell, where one ^{11}B atom is inserted into a Q^3 site, inducing framework condensations between next-nearest-neighboring Q^3 ^{29}Si sites.

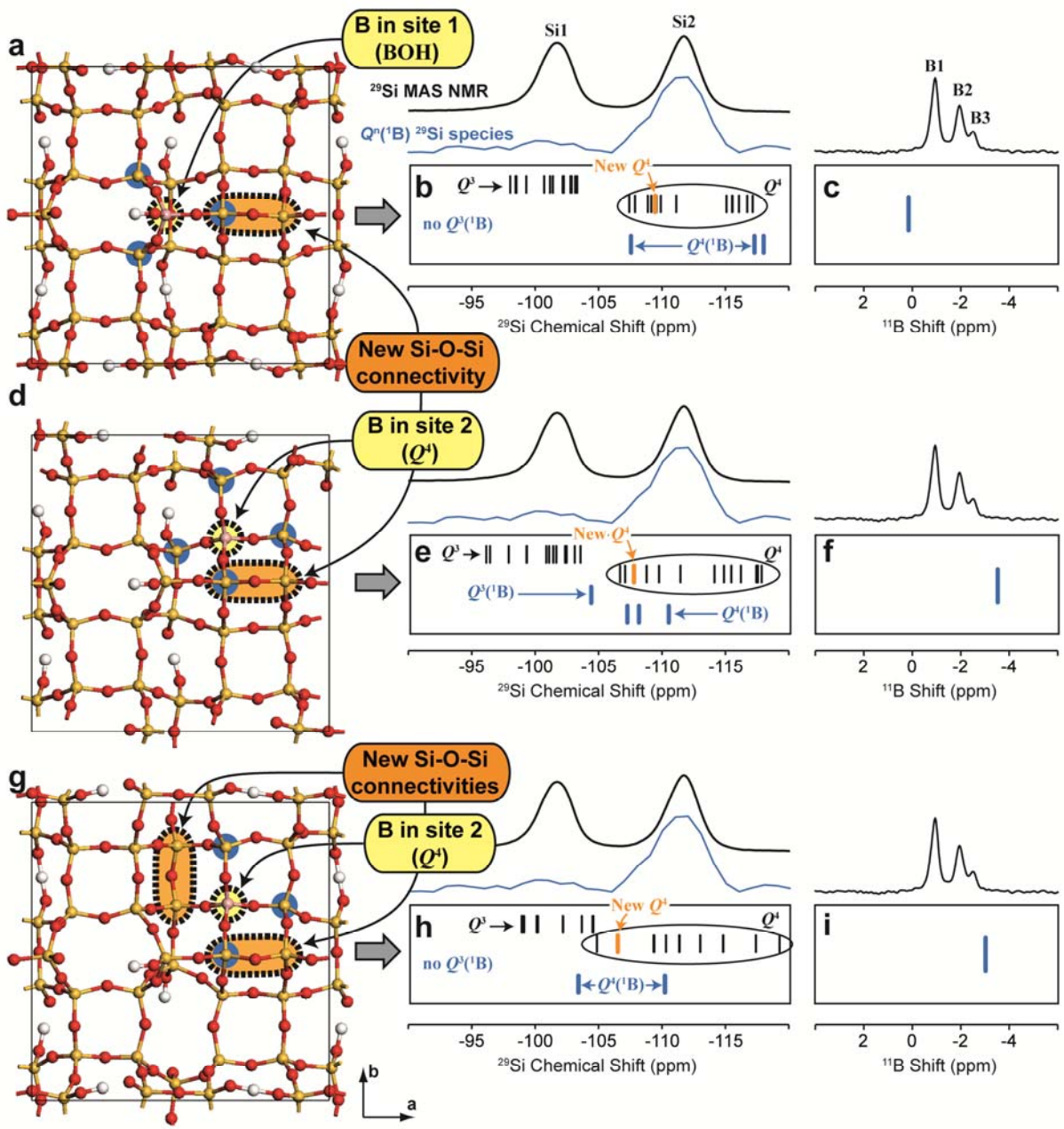

Figure 9. DFT-optimized structural models of $C_{16}H_{33}N^+$**Me$_3$**-directed layered borosilicates viewed from the c-axis, where ^{11}B atoms are manually inserted into ^{29}Si site (a) Si 1 or (d, g) Si2. For each structural model, 8 ^{1}H atoms per unit cell and other homogeneously distributed positive charges are included for charge compensation. Specifically, ^{11}B incorporation induces framework condensations between nearby Q^3 ^{29}Si sites to form (a, d) one or (g) two new ^{29}Si-O-^{29}Si site connectivities. Calculated isotropic chemical shifts for distinct ^{29}Si and ^{11}B species in the models (a), (d), and (g) are shown in plots (b, e, h) and (c, f, i), respectively, where the ^{29}Si chemical shifts in blue reveal the ^{29}Si species connected to one ^{11}B atom only. The calculated ^{29}Si chemical shifts in orange refer to newly formed Q^4 ^{29}Si species via framework condensations. Experimental ^{29}Si and ^{11}B MAS NMR spectra are shown along the top horizontal axis accordingly for reference.

REFERENCES.

1. K. Tanabe and W. F. Holderich, *Appl. Catal. A-Gen.*, 1999, **181**, 399-434.

2. M. Borja and P. K. Dutta, *Nature*, 1993, **362**, 43-45.

3. M. Iwamoto, H. Yahiro, N. Mizuno, W. X. Zhang, Y. Mine, H. Furukawa and S. Kagawa, *J. Phys. Chem.*, 1992, **96**, 9360-9366.

4. D. Barthomeuf, *Catalysis Reviews-Science and Engineering*, 1996, **38**, 521-612.

5. S. M. Kuznicki, V. A. Bell, S. Nair, H. W. Hillhouse, R. M. Jacubinas, C. M. Braunbarth, B. H. Toby and M. Tsapatsis, *Nature*, 2001, **412**, 720-724.

6. S. H. Joo, S. J. Choi, I. Oh, J. Kwak, Z. Liu, O. Terasaki and R. Ryoo, *Nature*, 2001, **412**, 169-172.

7. J. Choi, H.-K. Jeong, M. A. Snyder, J. A. Stoeger, R. I. Masel and M. Tsapatsis, *Science*, 2009, **325**, 590-593.

8. K. Varoon, X. Zhang, B. Elyassi, D. D. Brewer, M. Gettel, S. Kumar, J. A. Lee, S. Maheshwari, A. Mittal, C.-Y. Sung, M. Cococcioni, L. F. Francis, A. V. McCormick, K. A. Mkhoyan and M. Tsapatsis, *Science*, 2011, **333**, 72-75.

9. R. Bermejo-Deval, R. S. Assary, E. Nikolla, M. Moliner, Y. Roman-Leshkov, S. J. Hwang, A. Palsdottir, D. Silverman, R. F. Lobo, L. A. Curtiss and M. E. Davis, *Proc. Natl. Acad. Sci. U. S. A.*, 2012, **109**, 9727-9732.

10. J. Jae, G. A. Tompsett, A. J. Foster, K. D. Hammond, S. M. Auerbach, R. F. Lobo and G. W. Huber, *J. Catal.*, 2011, **279**, 257-268.

11. T. Willhammar, J. Sun, W. Wan, P. Oleynikov, D. Zhang, X. Zou, M. Moliner, J. Gonzalez, C. Martínez, F. Rey and A. Corma, *Nat Chem*, 2012, **4**, 188-194.

12. J. Dědeček, Z. Sobalík and B. Wichterlová, *Catalysis Reviews*, 2012, **54**, 135-223.

13. Y. Roman-Leshkov, M. Moliner and M. E. Davis, *J. Phys. Chem. C*, 2011, **115**, 1096-1102.

14. A. B. Pinar, C. Marquez-Alvarez, M. Grande-Casas and J. Perez-Pariente, *J. Catal.*, 2009, **263**, 258-265.

15. C. A. Hijar, R. M. Jacubinas, J. Eckert, N. J. Henson, P. J. Hay and K. C. Ott, *J. Phys. Chem. B*, 2000, **104**, 12157-12164.

16. C. Lamberti, S. Bordiga, A. Zecchina, G. Artioli, G. Marra and G. Spano, *J. Am. Chem. Soc.*, 2001, **123**, 2204-2212.

17. P. F. Henry, M. T. Weller and C. C. Wilson, *J. Phys. Chem. B*, 2001, **105**, 7452-7458.

18. M. Milanesio, C. Lamberti, R. Aiello, F. Testa, M. Piana and D. Viterbo, *J. Phys. Chem. B*, 2000, **104**, 9951-9953.

19. L. Palin, C. Lamberti, A. Kvick, F. Testa, R. Aiello, M. Milanesio and D. Viterbo, *J. Phys. Chem. B*, 2003, **107**, 4034-4042.

20. J. Shin, D. S. Bhange, M. A. Camblor, Y. Lee, W. J. Kim, I. S. Nam and S. B. Hong, *J. Am. Chem. Soc.*, 2011, **133**, 10587-10598.

21. J. A. van Bokhoven, T.-L. Lee, M. Drakopoulos, C. Lamberti, S. Thiesz and J. Zegenhagen, *Nat Mater*, 2008, **7**, 551-555.

22. E. Véron, M. N. Garaga, D. Pelloquin, S. Cadars, M. Suchomel, E. Suard, D. Massiot, V. Montouillout, G. Matzen and M. Allix, *Inorg. Chem.*, 2013, **52**, 4250−4258.

23. D. Massiot, R. J. Messinger, S. Cadars, M. Deschamps, V. Montouillout, N. Pellerin, E. Veron, M. Allix, P. Florian and F. Fayon, *Acc. Chem. Res.*, 2013, **46**, 1975-1984.

24. C. A. Fyfe, J. L. Bretherton and L. Y. Lam, *J. Am. Chem. Soc.*, 2001, **123**, 5285-5291.

25. S. Sklenak, J. Dedecek, C. B. Li, B. Wichterlova, V. Gabova, M. Sierka and J. Sauer, *Angew. Chem.-Int. Edit.*, 2007, **46**, 7286-7289.

26. O. H. Han, C. S. Kim and S. B. Hong, *Angew. Chem.-Int. Edit.*, 2002, **41**, 469-472.

27. J. Dedecek, L. Capek, P. Sazama, Z. Sobalik and B. Wichterlova, *Appl. Catal. A-Gen.*, 2011, **391**, 244-253.

28. J. Dedecek, V. Balgová, V. Pashkova, P. Klein and B. Wichterlová, *Chem. Mater.*, 2012, **24**, 3231-3239.

29. P. Sazama, J. Dedecek, V. Gabova, B. Wichterlova, G. Spoto and S. Bordiga, *J. Catal.*, 2008, **254**, 180-189.

30. C. Baerlocher, D. Xie, L. B. McCusker, S. J. Hwang, I. Y. Chan, K. Ong, A. W. Burton and S. I. Zones, *Nat. Mater.*, 2008, **7**, 631-635.

31. T. Willhammar, A. W. Burton, Y. Yun, J. Sun, M. Afeworki, K. G. Strohmaier, H. Vroman and X. Zou, *J. Am. Chem. Soc.*, 2014, **136**, 13570-13573.

32. D. Xie, L. B. McCusker, C. Baerlocher, L. Gibson, A. W. Burton and S. J. Hwang, *J. Phys. Chem. C*, 2009, **113**, 9845-9850.

33. A. Grünewald-Lüke, H. Gies, U. Müller, B. Yilmaz, H. Imai, T. Tatsumi, B. Xie, F.-S. Xiao, X. Bao, W. Zhang and D. De Vos, *Micropor. Mesopor. Mat.*, 2012, **147**, 102-109.

34. P. S. Neuhoff, S. Kroeker, L. S. Du, T. Fridriksson and J. F. Stebbins, *Am. Mineral.*, 2002, **87**, 1307-1320.

35. S. B. Hong, S.-H. Lee, C.-H. Shin, A. J. Woo, L. J. Alvarez, C. M. Zicovich-Wilson and M. A. Camblor, *J. Am. Chem. Soc.*, 2004, **126**, 13742-13751.

36. G. Engelhardt and D. Michel, *High-resolution solid-state NMR of silicates and zeolites*, Wiley, 1987.

37. K. J. D. Mackenzie and M. E. Smith, *multinuclear solid-state NMR of inorganic materials*, Pergamon Press, Oxford, 2002.

38. H. K. Jeong, S. Nair, T. Vogt, L. C. Dickinson and M. Tsapatsis, *Nat. Mater.*, 2003, **2**, 53-58.

39. T. Ikeda, Y. Akiyama, Y. Oumi, A. Kawai and F. Mizukami, *Angew. Chem.-Int. Edit.*, 2004, **43**, 4892-4896.

40. T. Ikeda, S. Kayamori and F. Mizukami, *J. Mater. Chem.*, 2009, **19**, 5518-5525.

41. L. Palin, G. Croce, D. Viterbo and M. Milanesio, *Chem. Mater.*, 2011.

42. B. Yilmaz, U. Muller, B. Tijsebaert, D. De Vos, B. Xie, F. S. Xiao, H. Gies, W. P. Zhang, X. H. Bao, H. Imai and T. Tatsumi, *Chem. Commun.*, 2011, **47**, 1812-1814.

43. Z. Li, B. Marler and H. Gies, *Chem. Mater.*, 2008, **20**, 1896-1901.

44. B. Marler and H. Gies, *Eur. J. Mineral.*, 2012, **24**, 405-428.

45. W. J. Roth, P. Nachtigall, R. E. Morris and J. Cejka, *Chem. Rev.*, 2014, **114**, 4807-4837.

46. S. C. Christiansen, D. Y. Zhao, M. T. Janicke, C. C. Landry, G. D. Stucky and B. F. Chmelka, *J. Am. Chem. Soc.*, 2001, **123**, 4519-4529.

47. N. Hedin, R. Graf, S. C. Christiansen, C. Gervais, R. C. Hayward, J. Eckert and B. F. Chmelka, *J. Am. Chem. Soc.*, 2004, **126**, 9425-9432.

48. Y. D. Xia and R. Mokaya, *Micropor. Mesopor. Mat.*, 2006, **94**, 295-303.

49. Y. D. Xia and R. Mokaya, *J. Phys. Chem. B*, 2006, **110**, 9122-9131.

50. G. Coudurier, A. Auroux, J. C. Vedrine, R. D. Farlee, L. Abrams and R. D. Shannon, *J. Catal.*, 1987, **108**, 1-14.

51. R. Millini, G. Perego and G. Bellussi, *Top. Catal.*, 1999, **9**, 13-34.

52. R. A. Van Nordstrand, D. S. Santilli and S. I. Zones, in *Molcular Sieves, Vol.1: Synthesis of Microporous Materials*, eds. M. L. Ocelli and H. E. Robson, New York, 1992, p. 373.

53. C. Y. Chen and S. I. Zones, Amsterdam, 2001.

54. D. Sakellariou and L. Emsley, in *Encyclopedia of Nuclear Magnetic Resonance*, eds. D. M. Grant and R. K. Harris, Wiley, London, 2002, vol. 9, pp. 196-211.

55. D. Massiot, F. Fayon, M. Deschamps, S. Cadars, P. Florian, V. Montouillout, N. Pellerin, J. Hiet, A. Rakhmatullin and C. Bessada, *C. R. Chim.*, 2010, **13**, 117-129.

56. C. A. Fyfe, H. Gies, Y. Feng and G. T. Kokotailo, *Nature*, 1989, **341**, 223-225.

57. C. A. Fyfe, H. Gies and Y. Feng, *J. Chem. Soc.-Chem. Commun.*, 1989, 1240-1242.

58. C. A. Fyfe, H. Gies and Y. Feng, *J. Am. Chem. Soc.*, 1989, **111**, 7702-7707.

59. S. Cadars, D. H. Brouwer and B. F. Chmelka, *Phys. Chem. Chem. Phys.*, 2009, **11**, 1825-1837.

60. C. A. Fyfe, K. C. Wongmoon, Y. Huang, H. Grondey and K. T. Mueller, *J. Phys. Chem.*, 1995, **99**, 8707-8716.

61. M. Deschamps, F. Fayon, J. Hiet, G. Ferru, M. Derieppe, N. Pellerin and D. Massiot, *Phys. Chem. Chem. Phys.*, 2008, **10**, 1298-1303.

62. P. Florian, E. Veron, T. F. G. Green, J. R. Yates and D. Massiot, *Chem. Mater.*, 2012, **24**, 4068-4079.

63. C. A. Fyfe, Y. Feng, H. Grondey, G. T. Kokotailo and H. Gies, *Chem. Rev.*, 1991, **91**, 1525-1543.

64. D. H. Brouwer, S. Cadars, J. Eckert, Z. Liu, O. Terasaki and B. F. Chmelka, *J. Am. Chem. Soc.*, 2013, **135**, 5641-5655.

65. S. Cadars, M. Allix, D. H. Brouwer, R. Shayib, M. Suchomel, A. W. Burton, G. M. N., A. I. Rakhmatullin, S. I. Zones, D. Massiot and B. F. Chmelka, *Chem. Mater.*, 2014, **26**, 6994-7008.

66. P. Florian, F. Fayon and D. Massiot, *J. Phys. Chem. C*, 2009, **113**, 2562–2572.

67. D. Massiot, F. Fayon, V. Montouillout, N. Pellerin, J. Hiet, C. Roiland, P. Florian, J. P. Coutures, L. Cormier and D. R. Neuville, *J. Non-Cryst. Solids*, 2008, **354**, 249-254.

68. J. Hiet, M. Deschamps, N. Pellerin, F. Fayon and D. Massiot, *Phys. Chem. Chem. Phys.*, 2009, **11**, 6935-6940.

69. G. De Paepe, N. Giraud, A. Lesage, P. Hodgkinson, A. Bockmann and L. Emsley, *J. Am. Chem. Soc.*, 2003, **125**, 13938-13939.

70. G. De Paepe, A. Lesage, S. Steuernagel and L. Emsley, *ChemPhysChem*, 2004, **5**, 869-875.

71. S. Vortmann, J. Rius, S. Siegmann and H. Gies, *J. Phys. Chem. B*, 1997, **101**, 1292-1297.

72. I. Wolf, H. Gies and C. A. Fyfe, *J. Phys. Chem. B*, 1999, **103**, 5933-5938.

73. N. Tsunoji, T. Ikeda, Y. Ide, M. Sadakane and T. Sano, *J. Mater. Chem.*, 2012, **22**, 13682-13690.

74. S. Cadars, N. Mifsud, A. Lesage, J. D. Epping, N. Hedin, B. F. Chmelka and L. Emsley, *J. Phys. Chem. C*, 2008, **112**, 9145–9154.

75. L. S. Du and J. F. Stebbins, *J. Non-Cryst. Solids*, 2003, **315**, 239-255.

76. C. Baerlocher, L. B. McCusker and D. H. Olson, *Atlas of Zeolite Framework Types*, Elsevier, Amsterdam, 2007.

77. S. I. Zones and S. J. Hwang, *Micropor. Mesopor. Mat.*, 2003, **58**, 263-277.

78. A. Boghoz, M. Soltanieh, R. Mondegarian and M. Karbalaee, *Industrial & Engineering Chemistry Research*, 1998, **37**, 2378-2382.

79. D. Iuga and A. P. M. Kentgens, *J. Magn. Reson.*, 2002, **158**, 65-72.

80. B. M. Fung, A. K. Khitrin and K. Ermolaev, *J. Magn. Reson.*, 2000, **142**, 97-101.

81. S. Hediger, B. H. Meier, N. D. Kurur, G. Bodenhausen and R. R. Ernst, *Chem. Phys. Lett.*, 1994, **223**, 283-288.

82. M. Carravetta, M. Eden, X. Zhao, A. Brinkmann and M. H. Levitt, *Chem. Phys. Lett.*, 2000, **321**, 205-215.

83. A. Brinkmann and M. H. Levitt, *J. Chem. Phys.*, 2001, **115**, 357-384.

84. A. Brinkmann and A. P. M. Kentgens, *J. Am. Chem. Soc.*, 2006, **128**, 14758-14759.

85. B. Hu, J. Trebosc and J. P. Amoureux, *J. Magn. Reson.*, 2008, **192**, 112-122.

86. A. Lesage, D. Sakellariou, S. Steuernagel and L. Emsley, *J. Am. Chem. Soc.*, 1998, **120**, 13194-13201.

87. S. J. Clark, M. D. Segall, C. J. Pickard, P. J. Hasnip, M. J. Probert, K. Refson and M. C. Payne, *Z. Kristallogr.*, 2005, **220**, 567-570.

88. J. P. Perdew, K. Burke and M. Ernzerhof, *Phys. Rev. Lett.*, 1996, **77**, 3865-3868.

89. D. Vanderbilt, *Phys. Rev. B*, 1990, **41**, 7892-7895.

90. H. J. Monkhorst and J. D. Pack, *Phys. Rev. B*, 1976, **13**, 5188-5192.

91. C. J. Pickard and F. Mauri, *Phys. Rev. B*, 2001, **63**, 245101.